

# Velocity Gradient in the Presence of Self-gravity: Identifying Gravity-induced Inflow and Determining Collapsing Stage

Yue Hu<sup>1,2</sup>, A. Lazarian<sup>2,3</sup>, and Ka Ho Yuen<sup>2</sup>

Department of Physics, University of Wisconsin-Madison, Madison, WI 53706, USA; yue.hu@wisc.edu

Department of Astronomy, University of Wisconsin-Madison, Madison, WI 53706, USA; alazarian@facstaff.wisc.edu

Korea Astronomy and Space Science Institute, Daejeon 34055, Republic of Korea

Received 2020 February 16; revised 2020 June 1; accepted 2020 June 2; published 2020 July 9

#### Abstract

Understanding how star formation is regulated requires studying the energy balance between turbulence, magnetic fields, stellar feedback, and gravity within molecular clouds. However, identifying the transition region where the gravity takes over remains elusive. Recent studies of the Velocity Gradient Technique (VGT), which is an advanced tool for magnetic field studies, reveal that the gradients of spectroscopic observables change their directions by 90° with respect to the magnetic fields in the regions of gravitational collapse. In this study, we perform 3D MHD numerical simulations. We observe that star formation successfully proceeds in strongly magnetized and fully ionized media. We confirm that the self-gravity induces the change of gradients' orientation and gradients' high amplitude. We explore two ways of identifying collapsing self-gravitating regions through the double-peak feature in the histogram of gradients' orientation and the curvature of gradients. We show that velocity gradients' morphology and amplitude can be synthetically used to trace the convergent inflows. By comparing with the column density Probability Density Functions method, we show that VGT is a powerful new tool for studying the gas dynamics and tracing magnetic field in star-forming regions. By analogy with VGT, we extend the Intensity Gradient Technique (IGT) to locate the gravitational collapsing region and shocks. We demonstrate that the synergy of VGT and IGT can determine the collapsing stages in a star-forming region.

Unified Astronomy Thesaurus concepts: Interstellar magnetic fields (845); Interstellar medium (847); Star formation (1569); Star forming regions (1565)

## 1. Introduction

The molecular clouds in Milky Way are permeated by ubiquitous turbulent magnetic fields (Larson 1981; Elmegreen & Scalo 2004; Ballesteros-Paredes et al. 2007; McKee & Ostriker 2007; Chepurnov & Lazarian 2009; Chepurnov et al. 2020; Zhang et al. 2020). Turbulence, magnetic fields, and gravity significantly impact the critical properties of the star formation processes and stellar initial mass distribution in molecular clouds (Parker 1965, 1979; Jokipii 1966; Kennicutt 1998a, 1998b; Li & Henning 2011; Hull et al. 2013; Andersson et al. 2015; Caprioli & Spitkovsky 2014). To understand the complex interplay of gravity, turbulence, and magnetic fields, it is essential to identify and study the transition regions where gravity takes over and collapse occurs (Shu 1977, 1992; Shu et al. 1994; Krumholz & McKee 2005; Hennebelle & Chabrier 2011; Padoan & Nordlund 2011; Federrath & Klessen 2012, 2013; Traficante et al. 2020; Xu & Lazarian 2020). Nevertheless, observational studies of the self-gravitating transition region in molecular clouds have still not yet been fully developed.

Most analytic star formation theories rely on the column density Probability Density Functions (N-PDFs) of supersonic, magnetized, and isothermal turbulence to gain insight regarding self-gravity (Vazquez-Semadeni et al. 1995; Klessen 2000; Robertson & Kravtsov 2008; Kritsuk et al. 2011; Collins et al. 2012; Padoan et al. 2017; Burkhart 2018). It was believed that in the presence of self-gravitating gas, the N-PDF evolves to a combination of log-normal format for low-density gas and a power-law tail for high-density gas (Vazquez-Semadeni et al. 1995; Robertson & Kravtsov 2008; Ballesteros-Paredes et al. 2011; Price et al. 2011; Collins et al. 2012; Burkhart 2018). The transition from log-normal to power-law N-PDF reveals the

density threshold, above which the gas is likely to become self-gravitating. However, in addition to self-gravity, the N-PDFs are also shaped into a power-law distribution due to the insufficient optical depth in self-absorbing media (Hu et al. 2020a) or the effects of line-of-sight contamination on the column density structure (Schneider et al. 2015a, 2015b; Law et al. 2019), as well as stellar feedback via ionization (Tremblin et al. 2014). The applicability of N-PDFs is therefore constrained.

The Velocity Gradient Technique (VGT) was initially developed as an advanced tool for magnetic field studies (González-Casanova & Lazarian 2017; Yuen & Lazarian 2017a; Hu et al. 2018; Lazarian & Yuen 2018). It uses the fact that within magnetohydrodynamic (MHD) turbulence, the turbulent eddies are anisotropic (Goldreich & Sridhar 1995) and their anisotropy reveals the local direction of the magnetic field that percolates the eddy (Lazarian & Vishniac 1999; Cho & Vishniac 2000). As a result, the velocity gradients of the eddies are perpendicular to the magnetic fields.

The ability of VGT to trace magnetic fields in turbulent media has been extensively tested in numerical simulations (Yuen & Lazarian 2017a; Hu et al. 2018; Lazarian et al. 2018; Yuen et al. 2018; Hsieh et al. 2019) as well as observations in, for example, molecular clouds (Hu et al. 2019b, 2019c) and neutral hydrogen gases (González-Casanova & Lazarian 2019; Hu et al. 2020b). Lazarian & Yuen (2018) and Hu et al. (2019c) have also revealed that a new effect takes place in the presence of self-gravity, which results in a new method for measuring the transition from strongly magnetized to gravitational collapsing gas. The matter infall induces a change of the direction of velocity gradients concerning the magnetic field. In other words, toward regions where star formation is taking place, the gradients of velocity observables induced by the infall motions

parallel to the magnetic field gradually begin dominating over the velocity gradients arising from turbulence. The observational signature of this change in the cloud dynamics is that the VGT orientation flips by up to 90° to align parallel with the direction of the magnetic fields (Yuen & Lazarian 2017b; Lazarian & Yuen 2018; Hu et al. 2019c).

By identifying the change of the velocity gradients, one can, therefore, identify the regions in which dynamics are dominated by self-gravity. If magnetic field direction is already known from polarimetry, this identification is trivial. However, the VGT was introduced as a technique for studying the magnetic field independently of high-cost and frequently impossible polarimetric studies. Therefore, in this paper, we discuss the pure applicability of VGT in identifying collapsing cloud regions as well as—very importantly—studying magnetic fields in self-gravitating molecular clouds.

One of the most important tools in identifying the signature of self-gravity in molecular clouds would be the use of N-PDFs. Our study of N-PDFs of of synthetic CO emissions in Hu et al. (2020a) has revealed that the shape of the N-PDFs will be skewed in the presence of self-absorption. This is a severe limitation of the N-PDFs. Moreover, even in the absence of the effects of radiation transfer, as we discuss in the following sections, VGT is a more sensitive tool compared to the N-PDFs, as VGT is sensitive to the convergent infall flows induced by the gravitational collapse. In addition, VGT can be used synthetically with intensity gradients that also change their orientation with respect to the magnetic field in the presence of self-gravity (Yuen & Lazarian 2017b; Hu et al. 2019a). However, the change of density field is an accumulating process, while the velocity field is significantly changed only when the gravitational energy dominates over the kinematic energy of turbulence. This helps to identify the stage of gravitational collapse for molecular clouds via the relative orientation of intensity gradients and velocity gradients. In addition, self-gravity induces high gradient amplitudes, but this is not the case for shocks. This high-amplitude feature paves the way to distinguish shocks and self-gravitating materials.

For this study, we use several computational tools that have been developed for gradient studies. For instance, to identify the boundary of the collapsing region, we develop a double-peak algorithm and also use the curvature algorithm presented in Yuen & Lazarian (2020). At the same time, we use Principal Component Analysis (PCA) to extract the most important channel map data from spectroscopic position—position—velocity (PPV) cubes (Hu et al. 2018). To find gradient directions, apart from the classical fixed size sub-block averaging (Yuen & Lazarian 2017a), we experiment with adaptive sub-block averaging (see Section 5.2). These methods improve the ways that the gradients are calculated.

The rest of the paper is structured as follows. In Section 2, we theoretically illustrate the properties of MHD turbulence in the presence and absence of self-gravity. In Section 3, we describe the full algorithm in calculating velocity gradients with the filtering process, i.e., the PCA. In Section 4, we give details about the numerical simulation used in this work. In Section 5, we study the responses of N-PDFs and velocity gradients with respect to self-gravity, and we identify gravitational collapsing regions. In Section 6, we extend our study of velocity gradients to intensity gradients and show how to determine collapsing stages and shocks. In Section 7,

we discuss the application and further development of VGT. In Section 8, we give our conclusions.

#### 2. Theoretical Consideration

# 2.1. VGT and MHD Turbulence Theory

The VGT utilizes the properties of MHD turbulence; in what follows, we explain those essential for understanding this technique (see Figure 1). A more detailed discussion of MHD turbulence can be found in a recent book by Beresnyak & Lazarian (2019).

The theory of MHD turbulence has been given a boost by the prophetic study by Goldreich & Sridhar (1995), denoted as GS95 hereafter. In particular, GS95 predicted the turbulent eddies to be anisotropic and showed that the degree of turbulence anisotropy increases as the scale of turbulent motions decreases (see Figure 1(b)). The subsequent study of turbulent reconnection in Lazarian & Vishniac (1999) demonstrated that turbulent reconnection of the magnetic field, which takes place over just one eddy turnover time, is an intrinsic part of the MHD turbulent cascade. The reconnection enables the mixing of magnetic field lines perpendicular to the magnetic field direction (see Figure 1(c)). The mixing motions within the eddies further induce changes of the fluid velocities perpendicular to the magnetic field lines (see Figure 1(d)). Therefore, the local gas velocity gradients are directed perpendicular to the local directions of the magnetic field.<sup>4</sup> This phenomenon has been confirmed by the numerical studies in Cho & Vishniac (2000) and Maron & Goldreich (2001). This notion of a local system of reference is critical for understanding the VGT. Indeed, for the detailed tracing magnetic field using the velocity field, it is essential that the velocities are oriented in respect to the direction of the magnetic field in the sampled volumes, rather than the direction of the mean magnetic field.

In the process of observations, the contributions from eddies of different scales are summed up. The smallest eddies trace the fine magnetic structure, while the larger eddies sample magnetic field on a coarser grid scale. For the VGT, it is essential that the gradients arising from the smallest eddies dominate. This follows from the scaling of MHD turbulence.

According to Lazarian & Vishniac (1999), magnetic fields give minimal resistance to the motions of eddies with scale  $l_{\perp}$  perpendicular to the local direction of the magnetic field, i.e., the magnetic field passing through the eddy at scale l. Thus, the eddies obey the hydrodynamic Kolmogorov law  $v_{l,\perp} \sim l_{\perp}^{\frac{1}{3}}$ , where  $v_{l,\perp}$  is the turbulence's injection velocity perpendicular to the local direction of the magnetic field. The relation between the scale  $l_{\parallel}$  along the magnetic field and  $l_{\perp}$  perpendicular the magnetic field is expressed as (Lazarian & Vishniac 1999):

$$l_{\parallel} \simeq L_{
m inj} \left( rac{l_{\perp}}{L_{
m inj}} 
ight)^{rac{2}{3}} M_{
m A}^{-rac{4}{3}}, \qquad \qquad (1)$$

where  $L_{\text{inj}}$  is the injection scale of turbulence and  $M_{\text{A}} = v_l/v_{\text{A}}$  is the Alfvénic Mach number, i.e., the ratio between the injection velocity  $v_l$  of turbulence and Alfvénic velocity  $v_{\text{A}}$ . By

<sup>&</sup>lt;sup>4</sup> The derivations in Goldreich & Sridhar (1995) for the anisotropy are done using the mean-field reference frame. The GS95 scaling is not observable in this mean-field frame.

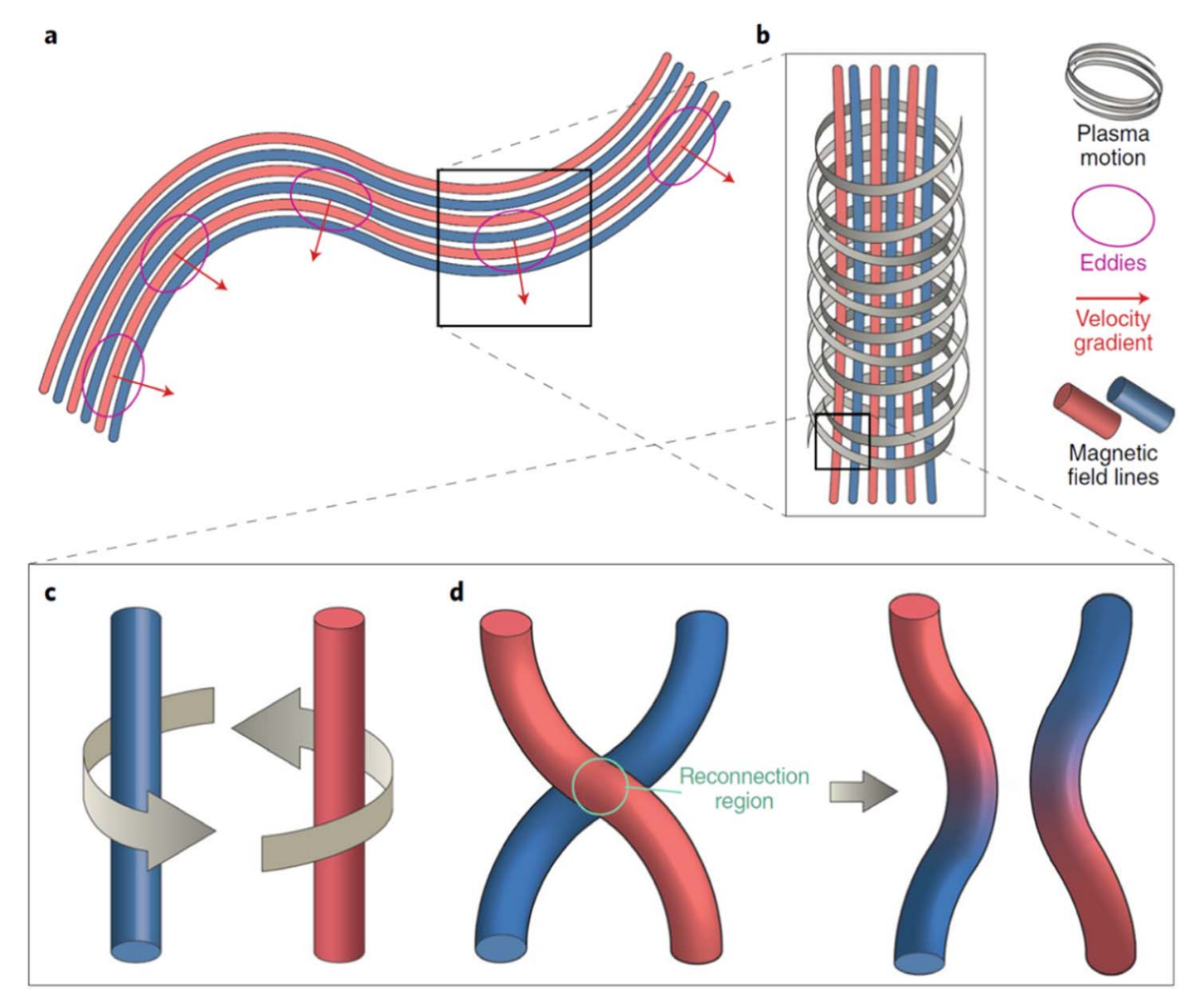


Figure 1. Cartoon extracted from Pattle (2019), explaining the principles behind the velocity gradient technique. Panel (a): the VGT technique considers Alfvénic fluid motions, wherein a magnetic field and the conducting fluid in which it is embedded move together. Panel (b): turbulent eddies are elongated along magnetic field lines. Panel (c): embedded magnetic field lines are preferentially moved perpendicular to their local direction by small-scale turbulent eddy motions. Panel (d): turbulent reconnection is an essential part of the dynamics of turbulent eddies, which enables the mixing of magnetic field lines perpendicular to the magnetic field direction. Mixing motions within the eddies (shown as magenta circles in panel (a)) induce changes of the fluid velocities perpendicular to the magnetic field lines. Therefore, local gas velocity gradients (red arrows in panel (a)) are directed perpendicular to the local directions of the magnetic field. As a result, it is possible to predict the direction of the magnetic field by measuring the direction of gas flow velocity gradients.

equating the period of Alfvénic wave and turbulent eddy's turnover time, the scaling of turbulent velocity of eddies is derived as (Lazarian & Vishniac 1999):

$$\frac{l_{\parallel}}{v_{\rm A}} \simeq \frac{l_{\perp}}{v_{l,\perp}} \tag{2}$$

$$v_{l,\perp} \simeq v_l \left(\frac{l_{\perp}}{L_{\rm inj}}\right)^{\frac{1}{3}} M_{\rm A}^{\frac{1}{3}} \tag{3}$$

when  $M_{\rm A}=1$  the relation returns to the GS95 version. Explicitly, because the anisotropic relation indicates  $l_{\perp}\ll l_{\parallel}$ ,

the velocity gradient scales as:

$$abla v_l \simeq rac{v_{l,\perp}}{l_\perp} \simeq rac{v_l}{L_{
m inj}} \left(rac{l_\perp}{L_{
m inj}}
ight)^{-rac{2}{3}} M_{
m A}^{rac{1}{3}}.$$
 (4)

Equation (4) is a crucial element for VGT technique, as it testifies that: (i) the gradients of velocity amplitude scale as  $v_{l,\perp}/l_{\perp} \propto l_{\perp}^{-2/3}$ , i.e., the smallest resolved scales are most important in calculating the gradients; and (ii) the measured velocity gradients are perpendicular to the magnetic field at the smallest resolved scales, i.e., they trace well the magnetic field in the turbulent volume.

b. a. Largest NET Local magnetic Local magnetic acceleration field direction field direction Velocity contours Direction of largest Largest centripetal Magnetic velocity gradient force required in 1 field lines direction resists compression ⊥ B-field

Figure 2. Illustrations of how self-gravity changes the maximum gradient direction, extracted from Yuen & Lazarian (2017b). Panel (a): eddies are elongated parallel to the local magnetic field direction. When gravity is absent (left), the maximum change of the velocity amplitudes (i.e., velocity gradient) is in the direction perpendicular to the local magnetic field. Panel (b): the gravitational pull produces the most significant acceleration of the plasma in the direction parallel to the magnetic field, and the velocity gradients are parallel to the magnetic field.

## 2.2. Velocity Gradient for Sub- and Super-Alfvénic Turbulence

Magnetized turbulent eddies

The magnetic field plays a crucial role in the anisotropic scaling relation, as shown in Equation (1). It is therefore important o discuss the turbulence scalings in different regimes, i.e., sub- and super-Alfvénic turbulence. We briefly describe the regimes below. A more extensive discussion can be found in the review by Brandenburg & Lazarian (2013).

For super-Alfvénic turbulence, the anisotropic relation appears when the scale of turbulence gets smaller than the transitional scale  $l_A$ , which is expressed as (Lazarian 2006):

$$l_{\rm A} = L_{\rm inj} M_{\rm A}^{-3}, M_{\rm A} > 1.$$
 (5)

At scales smaller than  $l_A$ , the turbulence transfers to the trans-Alfvénic turbulence described by the GS95 relation and the anisotropy of the turbulent eddies can be observed, i.e., Equation (3) still holds on. When turbulence's scale is larger than  $l_A$ , the turbulence cascade is essentially a hydrodynamic Kolmogorov cascade showing isotropic properties instead of anisotropic (Lazarian 2006).

In the strong magnetic field case  $M_{\rm A}$  < 1, the corresponding turbulence is always highly anisotropic. However, turbulence in the range from the injection scale  $L_{\rm inj}$  to transitional scale  $l_{\rm tr}$  becomes wave-like rather than eddy-like:

$$l_{\rm tr} = L_{\rm inj} M_{\rm A}^2, M_{\rm A} < 1,$$
 (6)

which is termed as weak Alfvénic turbulence (Beresnyak & Lazarian 2019). This type of turbulence means that the velocities change to (Lazarian & Vishniac 1999; Galtier et al. 2000):

$$v_{l,\perp} \simeq v_l \left(\frac{l_{\perp}}{L_{\rm inj}}\right)^{\frac{1}{2}},$$
 (7)

and the velocity gradient becomes:

Self-gravitating magnetized turbulent eddies

$$\nabla v_l \simeq \frac{v_{l,\perp}}{l_{\perp}} \simeq \frac{v_l}{L_{\rm inj}} \left(\frac{l_{\perp}}{L_{\rm inj}}\right)^{-\frac{1}{2}}$$
 (8)

At a scale smaller than  $l_{\rm tr}$ , the turbulence transforms into the strong Alfvénic regime, which obeys the GS95 anisotropic relation. In both regimes, the velocity gradients are perpendicular to the magnetic field. Note that turbulence can be also injected locally, whereupon the scale of turbulent motions  $L_{\rm inj}$  becomes different, as does  $l_{\rm A}$ . To trace the magnetic field direction using gradients, it is important that a telescope can resolve the turbulence at a scale smaller than  $l_{\rm A}$  for super-Alfvénic turbulence. In the case that resolution is not sufficient, the contribution from large scales should be removed using spatial filtering (Yuen & Lazarian 2017b).

# 2.3. Velocity Gradient in the Presence of Self-gravity

In the vicinity of gravitational collapse, the self-gravity radically modifies the nature of the turbulent flow. In the case of strong self-gravity, velocity gradients are expected to change their orientation from perpendicular to magnetic fields to align with magnetic fields (Yuen & Lazarian 2017b; Hu et al. 2019c). As shown in Figure 2, assuming the gravitational center is located at the center of a turbulent eddy, when gravity is subdominant to magnetic and turbulent energy, the magnetized turbulent eddies are elongated in the direction parallel to the magnetic field surrounding the eddies. As a result, the maximum change of the velocity amplitudes (i.e., velocity gradient), is in the direction perpendicular to the local magnetic field, and by rotating the velocity gradient by 90°, we can trace the magnetic field. In regions where gravitational collapse has begun, the dynamics are different. If the magnetic field is strong enough to

provide support, we expect that in the direction perpendicular to the magnetic field, any gravitational pull inducing the acceleration is counteracted by a magnetic force. Hence, the gravitational pull produces the most significant acceleration of the plasma in the direction parallel to the magnetic field, and the velocity gradients are parallel to the magnetic field. Alternatively, in a case where the magnetic field support is weak compared to gravity, the infall motions of the plasma will alter the magnetic field geometry such that it tends to align parallel to the direction of gravitational collapse. Nevertheless, the acceleration induced by the collapse is still along the magnetic field direction. As a result, the velocity gradients are also parallel to the magnetic field. In this paper, we focus on exploring the ability of VGT to trace magnetic field in the magnetically dominated environments with sub-Alfvénic turbulence. The turbulence in molecular clouds can be super-Alfvénic (Padoan & Nordlund 1999). In order to numerically study the applicability of the VGT in a super-Alfvénic setting, we require higher-resolution resolving scales less than the transitional scale  $l_A$ . The numerical study of the VGT for super-Alfvénic molecular clouds will be done elsewhere.

A similar argument also holds for intensity gradients, i.e., intensity gradients are perpendicular to the magnetic field due to the anisotropic relation of turbulent eddies. However, intensity gradients exhibit different properties from velocity gradients. A prior study in Soler et al. (2013) reported that the intensity gradient is rotating with respect to magnetic fields when arriving density threshold  $n_T \sim 50 \langle n \rangle$  (where  $\langle n \rangle$  denotes the average column density) in the case of  $M_s=10$  super-sonic media, and  $n_T \sim 500 \langle n \rangle$  in the case of moderately magnetized media ( $\beta=1.0$ ) for super-Alfvénic and self-gravitating MHD simulation. These findings are at the foundations of the Histograms of Relative Orientation (HRO) technique proposed in Soler et al. (2013) and elaborated further in Soler & Hennebelle (2017).

The difficulty of employing HRO compared to our way of identifying the gravitational collapse stems from two issues. First, HRO does not identify the change of the intensity gradients on its own. Instead, it requires polarization measurements to provide the magnetic field direction. Second, the change of the intensity gradient direction with respect to the magnetic field is also happening in the presence of shocks. Indeed, it has been demonstrated that the intensity gradient tends to be parallel to its local magnetic fields when getting close to the dense shock front in the absence of gravity (Yuen & Lazarian 2017b; Hu et al. 2019a; Xu et al. 2019). Therefore, the intensity gradient is sensitive to both self-gravity and shock. The change of intensity gradient induced by shocks does not specify a density threshold, which calls the value of  $n_T$  into question. Therefore, it encourages a detailed study of intensity gradients, i.e., distinguishing shocks and self-gravitating regions. In contrast, VGT provides, as we shall discuss further, a polarimetry-free way of determining self-gravitating regions. In addition, using the Intensity Gradient Technique (IGT), as we discuss later, there is a reliable way of distinguishing the shocks and self-gravitating regions

We note that, in this paper, we also use the intensity gradients. However, our IGT is *different* from the HRO (Hu et al. 2019a). The IGT is an offshoot of the VGT technique, and it uses the VGT procedures to trace magnetic field directions. In this paper, we show the synergy of using the VGT together with the IGT.

In this paper, we address the issue of how velocity gradients and IGs trace magnetic fields in the regions of self-dominant gravity for the case of sub- and trans-Alfvénic clouds, and further discuss how the stage of collapse is correlated to the alignment of density gradients and velocity gradients.

# 2.4. Distinguishing Shocks from Gravity in Spectroscopic Velocity Channels

Our previous works show that both regions with shock and those with self-gravity will cause the gradients of either intensity or centroid gradients to be parallel to the magnetic field (Yuen & Lazarian 2017b; Hu et al. 2019a). In this subsection, we formulate qualitatively how shocks are different from self-gravitating regions in velocity channel maps and how can we make use of this simple yet important principle to extract self-gravitating regions in observations.

In obtaining the velocity-gradient predicted magnetic field directions, we have to perform a weighted sum along the line of sight together with the magnetic field angle we predicted by VGT on channels. Shock and self-gravitating regions act differently under this "Stokes" sum (see Section 3): MHD shocks are mostly formed with its velocity dispersion being rather small. Therefore, when we are observing a shock region in PPV space, it occupies only a few velocity channels. Comparatively, the self-gravitating region accelerates fluid particles in its vicinity. That means when we are observing the self-gravitating region in PPV space, we can find this strongly self-gravitating region in almost all velocity channels.

This simple phenomenological effect has a profound consequence in searching for self-gravitating regions using velocity gradients. The shock density enhancement, unlike its self-gravity counterpart, is bounded by the sonic Mach number of the environment, but that for self-gravity is unbounded. In the case of shocks, there will be a limited number of channels that are affected by shocks, subject to the sonic Mach number. In this case, we will find most of the shocks in a limited amount of channels together with non-shock materials that have their gradients perpendicular to magnetic fields. As a result, for the channels with shocks, the alignment measure decreases, while for the channels without shocks, the alignment measure stays the same. Because our prediction of the magnetic field is a weighted sum along the line of sight, the effective alignment measure is only slightly decreased and is a function of  $M_s$ .

Self-gravity acts differently in velocity channels. We can find the self-gravitating region in all velocity channels, depending on its stage of collapse; as a result, the velocity gradients of every channel are rotated according to the strength of acceleration, causing the alignment of each channel to be significantly low. This would mean that, in the weighted sum, there are no channels that have an alignment measure high enough to counterbalance the gravity-induced low alignment measure channels, causing the resultant Stokes map to have a very low alignment measure. This means that only the change of orientation caused by gravity is retained under Stokes's addition. Therefore, using this simple fact, we can determine the self-gravitating regions by spotting the locations where there are changes of orientation of Stokes-weighted velocity gradients.

# 2.5. Velocity Fluctuations in the Thin Velocity Channel

Information about turbulent velocities is contained in PPV data, which are available through spectroscopic observations. The statistics of the intensity fluctuations in PPV and their relations to the underlying statistics of turbulent velocity and density are presented in Lazarian & Pogosyan (2000). There, it is shown the velocity effects are most prominent in thin channel maps, i.e., in thin velocity slices of PPV cubes.

Within thin channel maps, the field of velocity produces intensity fluctuations due to the effect of velocity caustics. These fluctuations in particular regimes identified in Lazarian & Pogosyan (2000) can dominate the effects of intensity fluctuations arising from density clumping. In fact, if the energy spectrum of magnetic fluctuations is steep (e.g., Kolmogorov spectrum), the velocity fluctuations determine the statistics of the intensities in thin channels (Lazarian & Pogosyan 2000). It can be demonstrated that this assumption holds not only in the single-phase self-absorption media but also in two-phase HI media (Lazarian & Pogosyan 2004; Kandel et al. 2016, 2017a, 2017b), provided that the cold HI clumps are moved together with the warm media. Therefore, by varying the thickness of velocity channels, one can extract the statistical density fluctuation and velocity fluctuation in PPV cubes (Lazarian 2009; Yuen et al. 2019). The criterion for distinguishing the thin channel and the thick channel is given as:

$$\Delta v < \sqrt{\delta v^2}$$
, thin channel  $\Delta v \geqslant \sqrt{\delta v^2}$ , thick channel, (9)

where  $\Delta v$  is the velocity channel width and  $\delta v$  is the velocity dispersion calculated from the velocity centroid (Lazarian & Pogosyan 2000). Therefore, we extract the velocity gradient from all thin channels that satisfy the criteria as listed in Equation (9).

However, in PPV cubes, only the velocity component parallel to LOS is achievable. If the flow induced by the gravitational collapse is exactly perpendicular to LOS and the flow does not allow the transfer of energy between different components, then there may be problems with detecting the velocity gradients change. However, in reality, it is not possible to accelerate the turbulent flow regularly in one direction without changing all the components of velocity. Differing from the convergent flow induced by the self-gravity, which spreads through space, shock only induces a jump of velocity in the direction perpendicular to the shocks' front and the velocity has limited range. Therefore, shocks' contribution to velocity field is insignificant in PPV cubes, as we discussed in Section 2.4.

Clark et al. (2019) recently questioned the validity of velocity caustics' effect in H I emission lines. They propose that the H I intensity features in thin channels are real density structures of the cold neutral medium instead of velocity caustics. The arguments of the authors are based on special properties of two-phase H I gas and are not applicable to the study of velocity gradients in isothermal conditions of molecular clouds that we deal in this paper. For a number of molecular clouds, we have obtained good correspondence of the magnetic field structure obtained from VGT and the one from Planck polarization data (Hu et al. 2019c) and from BLASTPOL polarization (Hu et al. 2019b).

A detailed discussion of the nature of the intensity fluctuations in channel maps for galactic H I studies is beyond the scope of the present paper. We shall only mention that the corresponding answer has been presented in Yuen et al. (2019). The fact is that the formation of velocity caustics predicted in Lazarian & Pogosyan (2000) theory is the effect that has been studied extensively, both theoretically and numerically, for the last two decades (Lazarian et al. 2001; Esquivel et al. 2003; Padoan et al. 2006; Chepurnov & Lazarian 2009; Kandel et al. 2017b; Clarke et al. 2018).

The predictions of the velocity caustic theory were successfully used to find the velocity spectrum by different groups in both two-phases HI media and one-phase media of CO isotopes,  $H_{\alpha}$ , N II, S II, and other species (Dickey et al. 2001; Stanimirović & Lazarian 2001; Khalil et al. 2006; Padoan et al. 2006; Kandel et al. 2017b). Therefore, it is an established fact that the velocity effects are important for the formation of intensity structure of the velocity channel maps. The discussion initiated by Clark et al. (2019) should be viewed in terms of the relative contributions of density and velocity for the production of the filaments observed in the channel maps. Realistic simulations of the two-phase media turbulence will clarify this issue. We also note that, by applying the VGT to HI data, we obtained predictions of foreground polarization that are in good correspondence with Planck measurements (Hu et al. 2020b).

# 2.6. Probability Density Function

The Probability Density Function (PDF) is one alternative way to identify gravitational collapsing regions by utilizing the information of the density field. Indeed, several studies have revealed that the density distribution is a log-normal  $(P_N)$  for supersonic magnetized isothermal turbulence (Vazquez-Semadeni et al. 1995; Robertson & Kravtsov 2008; Collins et al. 2012; Burkhart 2018):

$$P_N(s) = \frac{1}{\sqrt{2\pi\sigma_s^2}} e^{-\frac{(s-s_0)^2}{2\sigma_s^2}},$$
 (10)

where  $s = \ln(\rho/\rho_0)$  is the logarithmic density and  $\sigma_s$  is the standard deviation of the log-normal, while  $\rho_0$  and  $s_0$  denote the mean density and mean logarithmic density.

In the case of self-gravitating MHD turbulence, the gas density PDF evolves to a combination of log-normal  $(P_N)$  PDF at low densities and a power-law  $(P_L)$  PDF at high densities:

$$P_L(s) \propto e^{-\alpha s}, s > S_t,$$
 (11)

where  $S_t = \ln(\rho_t/\rho_0) = (\alpha - \frac{1}{2})\sigma_s^2$  is the logarithm of the normalized transitional density between the log-normal and power-law forms of the density PDF (Vazquez-Semadeni 1994; Slyz et al. 2005; Ballesteros-Paredes et al. 2011; Körtgen et al. 2019). The transition density  $S_t$  value depends on the slope  $\alpha$  of the power law and the width of the log-normal. As  $\alpha$  shallows (i.e., becomes less steep, which is expected for strong self-gravitating turbulence), the transition density ( $S_t$ ) between the PDF log-normal and power law moves toward lower density (Li 2018). Nevertheless, there still exist limitations of the N-PDFs in distinguishing regions of gravitational collapse in self-absorbing media, as discussed in Hu et al. (2020a).

#### 3. Methodology

# 3.1. Velocity Gradient Technique

The VGT initially employed either a velocity centroid map C(x, y) (González-Casanova & Lazarian 2017; Yuen & Lazarian 2017a) or a velocity channel map Ch(x, y) (Lazarian & Yuen 2018) to extract velocity information from PPV cubes:

$$C(x, y) = \frac{\int v \cdot \rho(x, y, v) dv}{\int \rho(x, y, v) dv}$$

$$Ch(x, y) = \int_{v_0 - \Delta v/2}^{v_0 + \Delta v/2} \rho(x, y, v) dv,$$
(12)

where  $\rho$  is gas density,  $\nu$  is the velocity component along the line of sight,  $\Delta \nu$  is the velocity channel width satisfied with Equation (9), and  $\nu_0$  is the velocity corresponding to the peak position in PPV's velocity profile. Note that both of these methods have had their validity tested by both numerical simulations (Yuen & Lazarian 2017a, 2017b; Lazarian & Yuen 2018; Hsieh et al. 2019) and observational data (Hu et al. 2019b, 2019c).

To improve the performance of VGT, Hu et al. (2018) used the Principal Component Analysis (PCA) as a tool to extract the most crucial n velocity components in a PPV cube. The implementation of PCA constructs a new orthogonal basis, which consists of n eigenvectors and n eigenvalues. The contribution from a principal component corresponding to small eigenvalues is also insignificant. Therefore, by omitting small eigenvalues and their corresponding principal components in the PPV cube, we can remove the noise. Also, it is possible to enhance the contribution from crucial components by projecting the original data set into the new orthogonal basis formed by the eigenvectors (Hu et al. 2018, 2020b). The PCA algorithm is implemented as follows.

As illustrated in Figure 3 ① ②, assuming that a PPV cube  $\rho$  (x, y, v) is a probability density function of three random variables x, y, v, we can obtain its covariance matrix and the eigenvalue equation for this covariance matrix from (Brunt & Heyer 2002a, 2002b; Hu et al. 2018, 2020b):

$$S(v_i, v_j) \propto \int dx dy \rho(x, y, v_i) \rho(x, y, v_j)$$

$$- \int dx dy \rho(x, y, v_i) \int dx dy \rho(x, y, v_j) \qquad (13)$$

$$S \cdot \mathbf{u} = \lambda \mathbf{u}, \qquad (14)$$

where S is the covariance matrix with matrix element  $S(v_i, v_j)$ , with  $i, j = 1, 2, ..., n_v$ .  $n_v$  is the number of channels in the PPV cubes, and  $\lambda$  represents the eigenvalues associated with the eigenvector  $\boldsymbol{u}$  (Hu et al. 2018, 2020b). By weighting channel  $\rho$   $(x, y, v_j)$  with the corresponding eigenvector element  $u_{ij}$ , we project the PPV cube into a new orthogonal basis, in which the corresponding eigen-map  $I_i(x, y)$  is:

$$I_i(x, y) = \sum_{i}^{n_y} u_{ij} \cdot \rho(x, y, v_j).$$
 (15)

Repeating the procedure for each eigenvector  $u_i$  results in a set of eigen-maps  $I_i(x, y)$ , with  $i = 1, 2, ..., n_v$  (see Figure 3 ③). From an individual eigen-map  $I_i(x, y)$ , the gradient orientation at individual pixel (x, y) is calculated by convolving the image

with  $3 \times 3$  Sobel kernels:

$$G_{x} = \begin{pmatrix} -1 & 0 & +1 \\ -2 & 0 & +2 \\ -1 & 0 & +1 \end{pmatrix}, \quad G_{y} = \begin{pmatrix} -1 & -2 & -1 \\ 0 & 0 & 0 \\ +1 & +2 & +1 \end{pmatrix}$$

$$\nabla_{x} I_{i}(x, y) = G_{x} * I_{i}(x, y)$$

$$\nabla_{y} I_{i}(x, y) = G_{y} * I_{i}(x, y)$$

$$\psi_{gi}(x, y) = \tan^{-1} \left( \frac{\nabla_{y} I_{i}(x, y)}{\nabla_{x} I_{i}(x, y)} \right), \quad (16)$$

where  $\nabla_x I_i(x, y)$  and  $\nabla_y I_i(x, y)$  are the x and y components of the gradients, respectively. Here,  $\psi_{gi}$  is the pixelized gradient map for each channel  $I_i(x, y)$  (see Figure 3  $\oplus$ ).

Note that, in the picture of turbulence, a single gradient in each pixel of  $\psi_{gi}$  contains little statistical information and does not directly indicate the magnetic field direction. However, the distributions of the gradient orientation appear as an accurate Gaussian profile with appropriate-sized subregions. Yuen & Lazarian (2017a) therefore proposed the sub-block averaging method, i.e., taking the Gaussian fitting peak value of the gradient distribution in a selected sub-block in order to statistically define the mean magnetic field in the corresponding subregion. Differing from Yuen & Lazarian (2017a), we continuously implement the sub-block averaging method. Each pixel of  $\psi_{gi}$  is taken as the center of a sub-block and the recipe of sub-block averaging is applied. The size of each sub-block is determined by the fitting errors within the 95% confidence level. We vary the sub-block size and check its corresponding fitting errors. When the fitting error reaches its minimum value, the corresponding sub-block size is the optimal selection. The resolution of the resulting gradient map is unchanged. We refer to this procedure as adaptive sub-block averaging (see Figure 3 4).

We denote the gradients' orientation after the adaptive sub-block averaging implemented as  $\psi_{gi}^s(x, y)$ . In analogy to the Stokes parameters of polarization, the pseudo  $Q_g$  and  $U_g$  of gradient-induced magnetic fields are defined as:

$$Q_{g}(x, y) = \sum_{i=1}^{n} I_{i}(x, y) \cos(2\psi_{gi}^{s}(x, y))$$

$$U_{g}(x, y) = \sum_{i=1}^{n} I_{i}(x, y) \sin(2\psi_{gi}^{s}(x, y))$$

$$\psi_{g} = \frac{1}{2} \tan^{-1} \left(\frac{U_{g}}{Q_{g}}\right). \tag{17}$$

The pseudo polarization angle  $\psi_g$  is then defined correspondingly, which gives a probe of plane-of-the-sky magnetic field orientation after rotating 90°. The rotation is automatically performed without specification (see Figure 3 ⑤). Note that, in constructing the  $Q_g(x,y)$  and  $U_g(x,y)$ , one can project the data onto the subset of the dominant principal components but not onto all of them, i.e.,  $n < n_v$ , especially when the smallest eigenvalues of the covariance matrix are dominated by noise (Hu et al. 2020b). The noise can be removed by eliminating the the smallest eigenvalues. Also, the pseudo-Stokes parameters is advantageous in correcting abnormal gradients vectors induced by either noise or fitting error. Lazarian & Yuen (2018) showed that magnetic field lines should be continuous, but an abnormal gradient vector cuts off the streamline compared to the

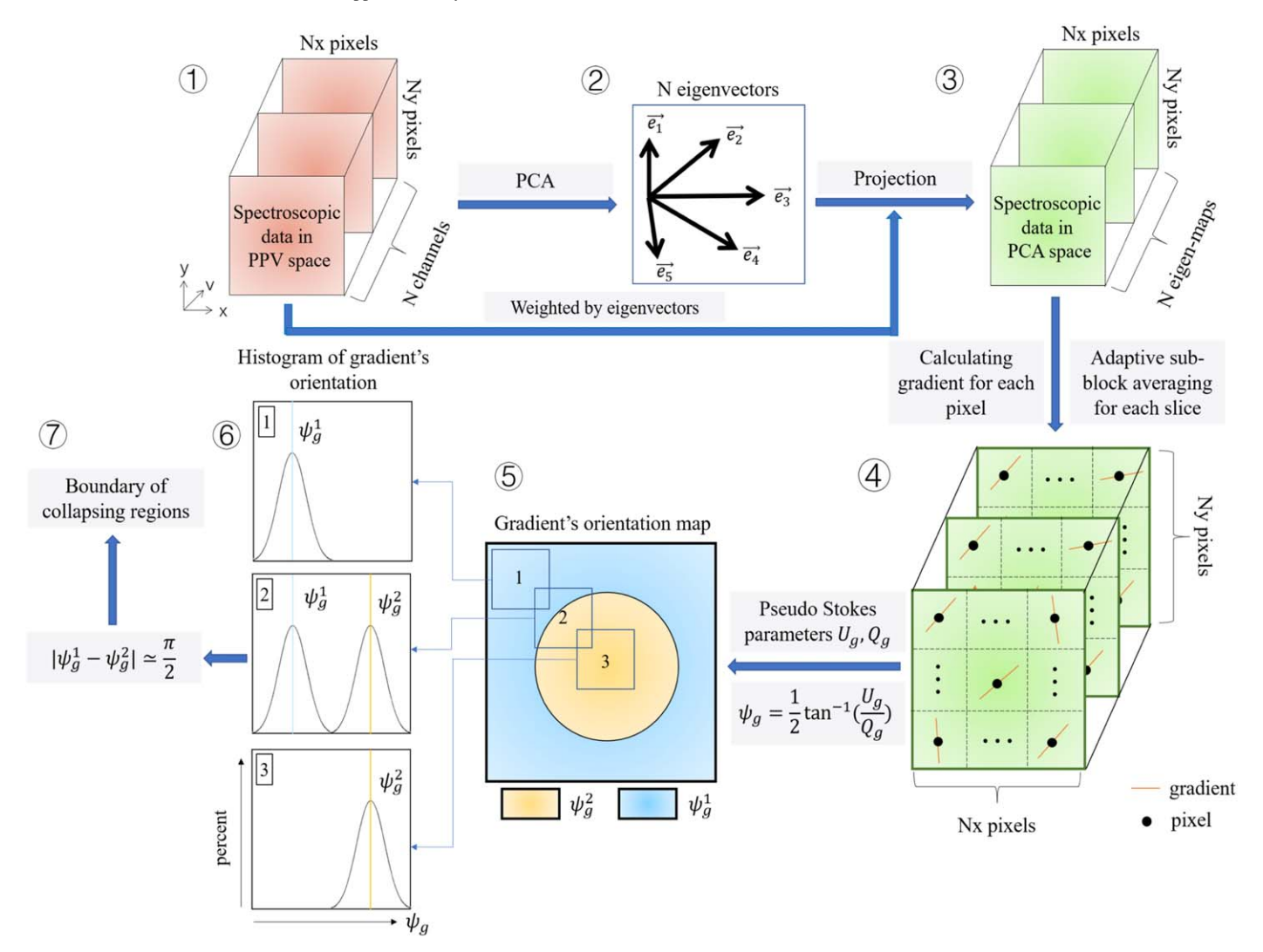


Figure 3. Diagram of the VGT procedure to identify the gravitational collapsing regions (see Section 3). Steps 1 to 3 cover preprocessing of the spectroscopic data with dimensions  $N_x \times N_y \times N$  via PCA. Assuming that a PPV cube  $\rho(x, y, v)$  is a probability density function of three random variables x, y, v, we can construct a new orthogonal coordinate system formed by the eigenvectors ( $e_1,e_2 \dots e_N$ ) of PPV's covariance matrix (see Equations (13) and (14)). By weighting the original PPV cube with the eigenvectors, we project the data into PCA's eigenspace. In the new space, the significance of important eddies is separated and signified. Step 4 and step 5 consist of constructing the pixelized 2D gradients map (see Equations (16) and (17)). With the preprocessed data cube, we calculate the per pixel gradients in each slice through the convolution with Sobel kernels. Per pixel gradient slice then is processed by the per pixel adaptive sub-block averaging method (see Section 5.2), which takes the Gaussian fitting peak value of the gradient distribution in a selected sub-block to statistically define the mean magnetic field in the corresponding subregion. This step outputs an  $N_x \times N_y \times N$  gradient cube. Final 2D gradient's orientation map results from the summation of the gradient cube, similarly to Stokes parameters (see Equation (17)). Step 6 and step 7 consist of identifying the boundary of gravitational collapsing regions through the double-peak algorithm (see Section 3.2). Based on theoretical considerations, gradients change their orientation by  $\pi/2$  in gravitational collapsing regions. Therefore, in diffuse region 1, we can see the gradient's histogram is approximately a single Gaussian distribution with the peak value located at  $\psi_g^1$ . In gravitationally collapsing region 3, the peak value of the histogram becomes  $\psi_g^2$ . However, in transitional region 2, the histogram appears bimodal, showing two peak values:  $\psi_g^1$  and  $\psi_g^2$ . Corresponding pixel is labeled as the boundary of the collaps

neighboring vectors. To smooth the outlying abnormal gradients, Lazarian & Yuen (2018) proposed the moving window method. In terms of the moving window method, a sub-block is selected to move along the orientation of the predicted magnetic field. When there is an abnormal gradient vector, a rotation is applied to the abnormal vector so that a smooth field line is formed. The moving window method is mathematically equivalent to the convolution of a Gaussian kernel with the cosine and sine angular components of the vectors. Nevertheless, Hu et al. (2019a) point out the nonlinear cosine or sine transformation distorts the Gaussian properties of

the vectors. The Gaussian convolution may further induce abnormal gradient vectors. In contrast, the pseudo-parameters recover the Gaussian distribution because of the weighting term  $I_i(x, y)$  (see Figure 10 in Hu et al. 2019a). Therefore, instead of smoothing directly the cosine and sine components, we propose that the Gaussian convolution can be applied to  $Q_g(x, y)$  and  $U_g(x, y)$ . In this work, as no noise is introduced to the numerical simulation, we do not distinguish the noise subset selecting  $n = n_v$  and do not employ the smoothing procedure.

The relative alignment between magnetic fields orientation and rotated pseudo polarization angle  $(\psi_g + \pi/2)$  is quantified

by the Alignment Measure<sup>5</sup> (AM):

$$AM = 2\left(\langle \cos^2 \theta_r \rangle - \frac{1}{2}\right),\tag{18}$$

where  $\theta_r$  is the angular difference in individual pixels, while  $\langle ... \rangle$  denotes the average within a region of interests. In the case of a perfect alignment of the magnetic field and VGT, we get AM=1, i.e., the global rotated  $\psi_g$  is parallel to the POS magnetic field, while AM=-1 indicates global rotated  $\psi_g$  is perpendicular to the POS magnetic field. The standard error of the mean gives the uncertainty  $\sigma_{AM}$ , i.e., the standard deviation divided by the square root of the sample size.

# 3.2. Double-peak Features in the Histogram of Velocity Gradients Orientation

To identify the boundary of collapsing regions from gradients' orientation, we developed the "double-peak algorithm," the essence of which we describe below. Based on our theoretical consideration, velocity gradients change their orientation by  $\pi/2$ in gravitational collapsing regions. This change can be extracted from the histogram of velocity gradients' orientation: (i) the single peak of the histogram locates at  $\theta$  in diffuse regions; (ii) the single peak of the histogram becomes  $\theta + \pi/2$  in gravitationally collapsing regions; and (iii) in the transitional region, i.e., the boundary of collapsing regions, the histogram is therefore expected to show two peak values  $\theta$  and  $\theta + \pi/2$ , denoted as a double-peak feature. As shown in Figure 4, the histogram of velocity gradients' orientation in the diffuse region shows a single-peak Gaussian profile, while in the boundary of the gravitational collapsing region, it shows a double-peak Gaussian profile. This distinct feature, therefore, gives information about gravitational collapsing regions. For magnetic field tracing, we perform a 90° rerotation to the gradients in the collapsing region. The resultant magnetic fields agree with the one inferred from synthetic polarization, i.e., AM = 0.75.

To implement the double-peak algorithm, we define every single pixel of  $\psi_g$  as the center of a sub-block and draw the histogram of velocity gradients orientation within this subblock (see Figure 3 6). Note the size of the sub-block can be different from the one for the sub-block averaging method (see Section 3.1) and we denote it as the second block. To suppress noise and the effect from an insufficient number of bins, we plot the envelope for the histogram, which is a smooth curve outlining its extremes. Any term whose histogram weight is less than the mean weight value of the envelope is masked. After masking, we work out the peak value of each consecutive profile. Once we have more than one peak value and the maximum difference of these peaks values is within the range  $90^{\circ} \pm \sigma_{\theta}$ , where  $\sigma_{\theta}$  is the total standard deviation of each consecutive profile, the center of this sub-block is labeled as the boundary of a gravitationally collapsing region (see Figure 3 ⑦).

# 3.3. The Curvature of Velocity Gradients

In addition to the double-peak algorithm, the curvature of velocity gradients can also be used to identify the boundary of collapsing regions. For a gravitationally collapsing region, velocity gradients rapidly change their direction by 90°. In this case, the curvature of velocity gradients reaches its maximum value on the boundary of the collapsing region, but the ambient region usually has small curvature. By sorting out the curvature, one can therefore find the boundary of self-gravitating regions. Note that, to have the best performance, the calculation of the velocity gradient should satisfy Equation (9). Otherwise, the contribution from density may be significant.

To calculate the curvature, we follow the precedent of Yuen & Lazarian (2020) by considering the magnetic field lines to be the velocity field of an imaginary particle. We first interpolate the pixelized gradient field  $\psi_g$ . Next, a second-order Runge–Kutta (RK2) vector integrator is implemented to produce a sufficient stream path that allows us to compute the curvature directly.

The method of RK2 vector integration can be easily implemented. Given a vector field  $\psi_g(x, y)$  and step size dt, where  $(x, y) \in R$ , for example, we can produce the next two coordinates (x', y') and (x'', y'') along the stream path of gradients as:

$$(x', y') = (x, y) \pm \psi_{g}(x, y) * dt/2$$
 (19)

$$(x'', y'') = (x, y) \pm \psi_g(x', y') * dt/2,$$
 (20)

where the plus sign means a forward integrator and minus sign is a backward integrator. We perform the integrator forward and backward, respectively, for four steps each, to establish a streamline  $L(t) = \{(x_i, y_i, t)\}_{i \in N}$  for each pixel, where t is the parameterized variable defining the streamline. Then we can compute the unsigned curvature  $\kappa(t)$  through the definition (Coolidge 1952):

$$T(t) = \frac{\dot{L}(t)}{|\dot{L}(t)|}$$

$$\kappa(t) = |\dot{T}(t)|. \tag{21}$$

Because the computation of T(t) requires a normalization, we then will first obtain the normalized T. The derivative of T(t) is computed using the one-dimensional five-point stencil:

$$\dot{T}_x(t) = \frac{-T_x(t+2dt) + 8T_x(t+dt) - 8T_x(t-dt) + T_x(t-2dt)}{12dt}$$

$$\dot{T}_y(t) = \frac{-T_y(t+2dt) + 8T_y(t+dt) - 8T_y(t-dt) + T_y(t-2dt)}{12dt}.$$
(22)

By repeating this recipe for every pixel in the map, we can create a pixelized 2D curvature map of the gradient field  $\psi_g(x, y)$ . When there exists a 90° change of gradients,  $\kappa(t)$  obtains its maximum value.

# 4. MHD Simulation Data

We perform 3D MHD simulations through the ZEUS-MP/3D code (Hayes et al. 2006), which solves the ideal MHD equations in a periodic box. We use single-fluid, operator-split, solenoidal turbulence injections and staggered-grid MHD Eulerian assumption. To emulate part of an interstellar cloud, we use the

<sup>&</sup>lt;sup>5</sup> The alignment measure given by Equation (18) was introduced in analogy with the grain alignment research (see Lazarian 2007) in González-Casanova & Lazarian (2017) and then was used in all the subsequent publications by our group. It has also been borrowed by other groups, e.g., for doing the Histogram of Oriented Gradients (Soler et al. 2019) and the Rolling Hough Transform (Clark & Hensley 2019).

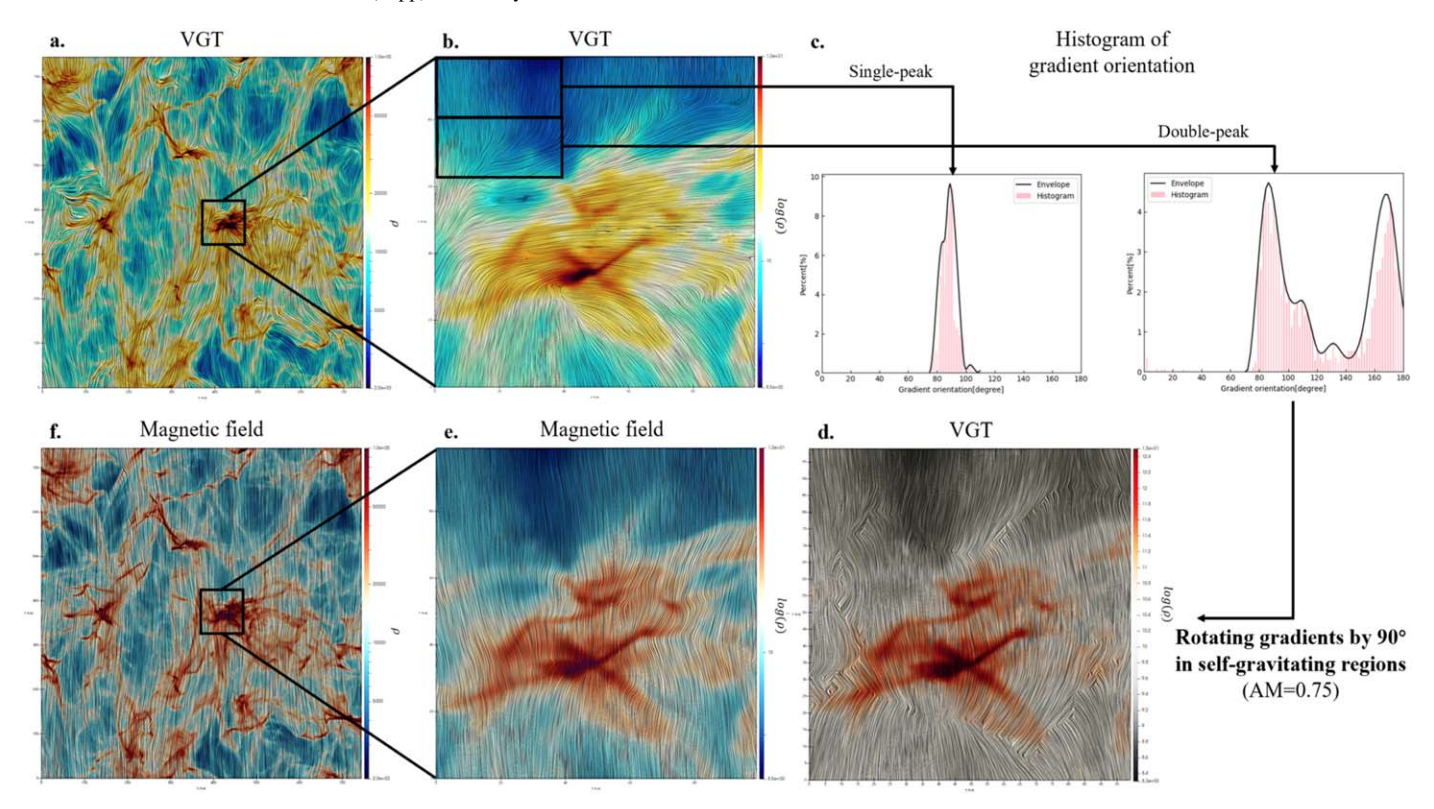


Figure 4. Example of how velocity gradients change orientations at the gravitational collapsing region, using simulation A1 with  $t_r \simeq 0.8$  Myr (see Table 1). Panels (a) and (b): a global and a zoom-in magnetic field morphology respectively inferred from VGT. Magnetic field is superimposed on the projected intensity map and visualized using the Line Integral Convolution (LIC). LIC is plotted using Paraview's default setting with steps 40 and step size 0.25. Panels (f) and (e): a global and a zoom-in magnetic field morphology respectively inferred from synthetic polarization. Panel (c): histogram of velocity gradients' orientation in the diffuse region, which shows a single-peak Gaussian profile (left), and in the boundary of the gravitational collapsing region, which shows a double-peak Gaussian profile (right). This same region has been shown to be gravitationally collapsing in Figure 13 through the N-PDFs. Panel (d): zoom-in magnetic field morphology inferred from VGT with a 90° rerotation implemented for the gravitationally collapsing region; corresponding AM is 0.75.

barotropic equation of state, i.e., these clouds are isothermal, with temperature  $T=10.0\,\mathrm{K}$ , sound speed  $c_s=187\,\mathrm{m\,s^{-1}}$ , and cloud size  $L=10\,\mathrm{pc}$ . The sound-crossing time  $t_v=L/c_s$  is  $\sim 52.0\,\mathrm{Myr}$ , which is fixed owing to the isothermal equation of state.

MHD turbulence is characterized by sonic Mach number  $M_s = v_l/c_s$  and Alfvénic Mach number  $M_A = v_l/v_A$ , where  $v_l$  is the injection velocity and  $v_A$  is the Alfvénic velocity. The turbulence is highly magnetized when the magnetic pressure of plasma is larger than the thermal pressure, i.e.,  $M_A < 1$ . The compressibility of turbulence is characterized by  $\beta = 2\left(\frac{M_A}{M_s}\right)^2$ . We refer to the simulations in Table 1 by their model names. For instance, each of our figures will have a model name indicating which data cube was used to plot the figure. The total mass  $M_{\rm tot}$  in the simulated cubes A1 is  $M_{\rm tot} \sim 18430.785~M_{\odot}$ , the magnetic Jean mass is  $M_{\rm JB} \sim 286.95~M_{\odot}$ , average magnetic field strength is  $B \sim 30.68~\mu{\rm G}$ , mass-to-flux ratio is  $\Phi \sim 1.11$ , and volume density is  $\rho \sim 318.32~{\rm cm}^{-3}$ . As for A2, we have  $M_{\rm tot} \sim 32765.74~M_{\odot}$ ,  $M_{\rm JB} \sim 96.68~M_{\odot}$ ,  $B \sim 31.33~\mu{\rm G}$ ,  $\Phi \sim 1.92$ , and volume density  $\rho \sim 565.90~{\rm cm}^{-3}$ . Based on the initial setting parameters, the intrinsic freefall time  $t_{\rm ff}$  is  $\sim 1.88~{\rm Myr}$  and  $1.40~{\rm Myr}$  for simulations A1 and A2, respectively.

The self-gravitating module, which employs a periodic Fast Fourier Transform Poisson solver, is switched on after turbulence inside the cube becomes saturated and the simulation has run for at least two sound crossing times. The scale of the simulation has 10 pc represented by 792 and 480 pixels for A1 and A2, respectively. The thermal Jeans length, therefore,

occupies 94 pixels (1.18 pc for A1) or 45 pixels (0.89 pc for A2). We keep driving both turbulence and self-gravity until the simulation violates the Truelove criterion (Truelove et al. 1997), which requires that the self-gravitating core should occupy at least four pixels. The density, therefore, can be enhanced by a factor of  $\sim\!552$  (A1) or  $\sim\!127$  (A2) times, i.e., we can have maximum volume density  $\rho_{\rm max}\sim 175712.63~{\rm cm}^{-3}$  for A1, while  $\rho_{\rm max}\sim 71869.30~{\rm cm}^{-3}$  for A2, which informs us when to stop the simulation before having numerical artifacts due to self-gravitational collapse.

# 5. Results

# 5.1. Evolution of the Probability Density Functions

To examine the behavior of the PDF at different collapsing stages, we apply it to 18 snapshots of A2 for each interval of the evolution time  $\Delta t_r = 0.20$  Myr, after the gravity is turned on. In Figure 5, we plot the density PDF for simulation A2. The N-PDFs are fitted within a 95% confidence level from initial data analysis. Figure 5(a) shows that the N-PDFs are in log-normal format until  $t_r = 2.2$  Myr, while the width of the N-PDFs is increasing. The prior studies (Krumholz & McKee 2005; Burkhart et al. 2009) explained that, for isothermal turbulence, the width of log-normal N-PDFs is given by  $M_s$  and turbulence driving parameter b:

$$\sigma_s^2 = \ln(1 + b^2 M_s^2). \tag{23}$$

Theoretically,  $\sigma_s$  should include the contribution from the magnetic field. However,  $\sigma_s$  is an auxiliary method for our

 Table 1

 Description of Our MHD Simulations

Model	$M_s$	$M_{ m A}$	$\beta = 2\left(\frac{M_A}{M_c}\right)^2$	Resolution	t <sub>r</sub> (Myr)
	5.64	0.31	0.006	792 <sup>3</sup>	0
	6.03	0.31	0.005	$792^{3}$	0.2
A1	6.23	0.31	0.005	$792^{3}$	0.4
	6.41	0.31	0.005	$792^{3}$	0.6
	6.52	0.31	0.004	$792^{3}$	0.8
	0.20	0.02	0.020	480 <sup>3</sup>	0
	0.20	0.02	0.020	$480^{3}$	0.2
	0.21	0.02	0.018	$480^{3}$	0.4
	0.25	0.02	0.013	$480^{3}$	0.6
	0.29	0.03	0.021	$480^{3}$	0.8
	0.35	0.03	0.015	$480^{3}$	1.0
	0.42	0.04	0.018	$480^{3}$	1.2
	0.52	0.04	0.012	$480^{3}$	1.4
A2	0.63	0.05	0.013	$480^{3}$	1.6
	0.77	0.06	0.012	$480^{3}$	1.8
	0.94	0.08	0.014	$480^{3}$	2.0
	1.16	0.10	0.015	$480^{3}$	2.2
	1.43	0.12	0.014	$480^{3}$	2.4
	1.77	0.14	0.013	$480^{3}$	2.6
	2.20	0.17	0.012	$480^{3}$	2.8
	2.71	0.21	0.012	$480^{3}$	3.0
	3.31	0.24	0.010	$480^{3}$	3.2
	3.97	0.27	0.010	$480^{3}$	3.4

**Note.** The self-gravitating module is switched on at the beginning, i.e., running time  $t_r$  is 0. We take a snapshot of the simulation every 0.2 Myr. Here,  $M_s$  and  $M_A$  are the instantaneous values at each snapshot.

paper, which is dealing with gradients. We do not provide a dedicated study of this quantity in this paper. In any case, this equation is widely used in many MHD studies (Vazquez-Semadeni et al. 1995; Robertson & Kravtsov 2008; Ballesteros-Paredes et al. 2011; Price et al. 2011; Collins et al. 2012; Burkhart 2018), so we keep it in the original form. In this situation, we expect that A2 will tend to be supersonic with the increment of self-gravity, and we do see the  $M_s \geqslant 1$  after  $t_r > 2.0$  Myr. Note that, although the fitted N-PDFs in Figure 5(a) are log-normal, fewer parts of unfitted N-PDFs are similar to a power-law format. One explanation for this may be that the small volume gravitational center becomes self-gravitating earlier.

Figure 5(b) shows that the N-PDFs of A2 with  $t_r \ge 2.4$  Myr. We see the N-PDFs become the combination of a log-normal component for low-density gas and a power-law component for high-density gas. The increasing  $\sigma_s$  also indicates that the  $M_s$  of simulation A2 is continuously growing. The gas within the power-law part is expected to be self-gravitating. The shallower slope  $\alpha$  and the smaller value of transitional density  $S_t$  reveal that the volume of self-gravitating gas is increasing (Collins et al. 2012; Burkhart 2018).

However, the supersonic simulation A1 behaves differently in the presence of self-gravity. The power-law part appears at  $t_r \leq 0.2$  Myr. The transition from an overall log-normal N-PDF to a hybrid (i.e., the combination of a log-normal part and a power-law part) PDF disappears for A1. Slope  $\alpha$  gets shallower, and the value of transitional density  $S_t$  becomes smaller with the evolution. The width of the log-normal part increases insignificantly. We then expect the volume of gravitationally collapsing

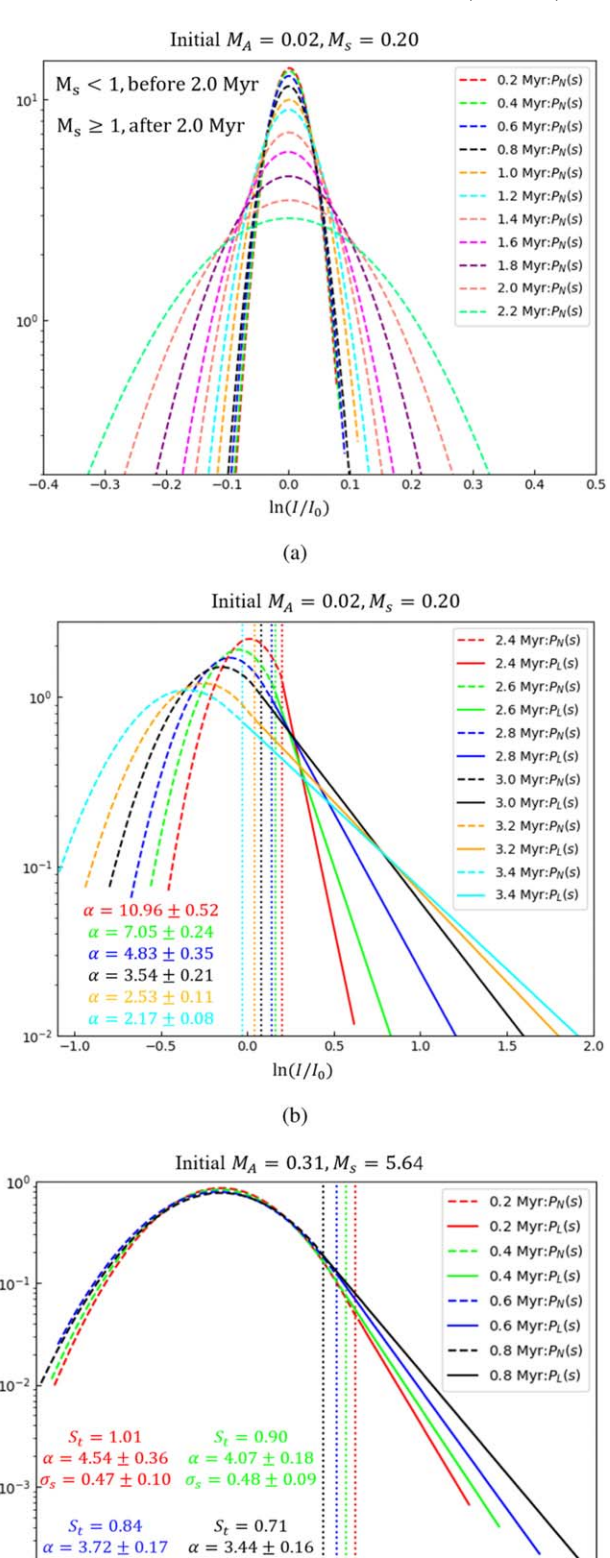


**Figure 5.** Log-normal plus power-law models of normalized PDF with bin size 100. Dotted line outlines all the density past the transition density, which is the dense self-gravitating gas. Here,  $\alpha$  is the slope of the power-law part,  $I_0$  is the mean intensity value,  $S_t$  denotes the transition density, and  $\sigma_s$  represents the standard deviation of the log-normal part.

 $ln(I/I_0)$ 

(c)

 $\sigma_s = 0.51 \pm 0.09$   $\sigma_s = 0.53 \pm 0.14$ 

gas to be small, such that it contributes little to the overall supersonic gas.

## 5.2. Adaptive Sub-block Averaging

In order to identify the gravitational collapsing region, a highresolution gradient map produced by VGT is indispensable. In Yuen & Lazarian (2017a), the velocity gradient calculation requires the use of a *sub-block* that would eventually degrade the input observable map in order to have a statistically viable magnetic field prediction. The size of such a block has to be large enough to obey the statistical requirement (which is the Gaussian fitting requirement) as listed in Yuen & Lazarian (2017a) and Lazarian & Yuen (2018), but not too large, so that most of the information is retained. For our particular purpose in this paper, we are more concerned with the signature of gravitational collapse in the observables. As we know from previous works (Yuen & Lazarian 2017b; Lazarian & Yuen 2018; Hu et al. 2019a), a large fixed block size would provide low spatial resolution and may miss the small gravitational collapsing region in which the gradients flip their direction. It is inevitable that we need a block averaging algorithm that can provide a high-resolution magnetic field output yet not violate the statistical requirement as posted in Yuen & Lazarian (2017a).

Therefore, in the current work, we introduce an algorithm called adaptive sub-block averaging. Pictorially for a selected pixel on the sky, a rectangular box is constructed with the selected pixel at the center. By increasing the size of the subblock, we can obtain a better fit in terms of the squared error of the Gaussian statistics requirement, as listed in Yuen & Lazarian (2017a) under 95% confidence. We shall pick that as the "optimal block size" for that pixel. This fitting procedure will ensure that: (1) each pixel will have a block size for later statistical purposes and (2) the output magnetic field and the input observable map have comparable resolutions. Although this procedure is similar to the convolution with a kernel, it takes the peak value of the fitted Gaussian curve rather than adding each element of the image to its local neighbors, weighted by the kernel. Without specification, we adopt the adaptive sub-block averaging method in what follows. It is worth remarking that the Gaussian fitting requirement in Yuen & Lazarian (2017a) can be replaced by a more theoretically driven cosine fitting requirement, as suggested by Lu et al. (2020).

In Figure 6, we compare the adaptive sub-block averaging method with the old version, i.e., fixed sub-block size, using simulation A1 at  $t_r \simeq 0.8$  Myr. We can clearly see that the adaptive sub-block averaging method outputs a magnetic field map with higher resolution than that of the fixed sub-block (size = 44 pixels). We calculate the AM between the rotated velocity gradients and magnetic fields. For the fixed sub-block averaging, we vary the block size from 22 to 33, 44, and 66. We can see the AM is increasing from 0.625 to 0.825 with the increment of block size. If we implement the adaptive sub-block averaging method, the AM is approximately 0.73, which is similar to the case where the fixed block size is 40 pixels. Note that the adaptive block method does not trace per pixel magnetic field, but rather the mean magnetic field within approximately the effective block. The effective block size gives the global mean resolution of the magnetic field resolved by VGT. Importantly, the adaptive sub-block averaging method guarantees the gradient map sufficiently high resolution for the implementation of the double-peak algorithm, as we will discuss in Section 5.6.1.

# 5.3. The Change of Velocity Gradients' Orientation

Velocity gradients are expected to change their relative orientation with respect to magnetic fields in the presence of gravitational collapse. To study the significance of gravity in the properties of gradients, we further explore the evolution of gradients with regard to different stages of gravitational collapse by taking eighteen snapshots for simulation A2. We calculate the AM of rotated gradients and magnetic fields. The results are shown our in Figure 7(a). At the time  $t_r = 0$ , gravity has been introduced into the simulation that already stirred with magnetized turbulence, and we take the snapshot until  $t_r \simeq 3.4 \, \mathrm{Myr}$ . At  $t_r \simeq 2.4 \, \mathrm{Myr}$ , the AM falls below zero. After this, the negative AM indicates that most of the rotated gradient vectors tend to be orthogonal to the magnetic field direction. To confirm that this change is induced by gravitational collapse, an estimation of the collapsing material is necessary. However, a cloud may not be collapsing because of the support of the magnetic field and turbulence, even if the gravitation energy is large. A more reliable measurement of collapsing gas is the convergence of the 3D velocity field, since when there exists gravitational collapse, flows of matter are converging into the collapsing center. As a result, the convergence of velocity is expected to increase significantly. We then calculate the convergence C, which is defined as the negative divergence of velocity:

$$\mathfrak{C} = -\nabla \cdot \mathbf{v} = -\left(\frac{\partial v_x}{\partial x} + \frac{\partial v_y}{\partial y} + \frac{\partial v_z}{\partial z}\right),\tag{24}$$

where  $v_x$ ,  $v_y$ ,  $v_z$  are the x, y, z components of the 3D velocity field respectively. We project it along the line of sight into a 2D map. Since the projection sums up all divergence and convergence, a positive 2D convergence is expected to indicate the dominance of convergent flow in 3D. In Figure 7(b), we plot the correlation of the mean projected convergence and gravitational energy. We can see that convergence is positively proportional to the increment of gravitational energy. The supersonic convergent fluid is, therefore, induced by self-gravity. Also, in Figure 7(c), we show the variation of magnetic field energy, kinetic energy, and gravitational energy  $|E_g|$ . We find kinetic energy  $E_k$  and gravitational energy are both increased because the self-gravity is accelerating the convergent flow. The energy relation approximately satisfies  $|E_g| \simeq 2E_k$ . However, the magnetic energy is keeping approximately constant, which is the result of turbulence reconnection. The reconnection diffusion tends to make the magnetic distribution uniform and uncorrelated with the density enhancement (Lazarian et al. 2020).

According to our theoretical consideration in Section 2, the convergent flow shall follow the magnetic field line. In Figure 7(d), we calculate the AM of magnetic field angle and velocity angle in 3D Position–Position–Position space. We see the AM is increasing from -0.2 to +0.6 with the increment of freefall time, i.e., gravitation energy. This implies that the velocity field is becoming parallel to the magnetic field. As the convergent fluid is following the same direction as velocity, the convergent flow is also parallel to the magnetic field in the case of gravitational collapse. This agrees with our theoretical consideration. Also, at the full range of evolution time, the magnetic field energy is always more significant than others.

In addition, we apply the second-order correlation function to the projected intensity map I(x, y) at different snapshots. This

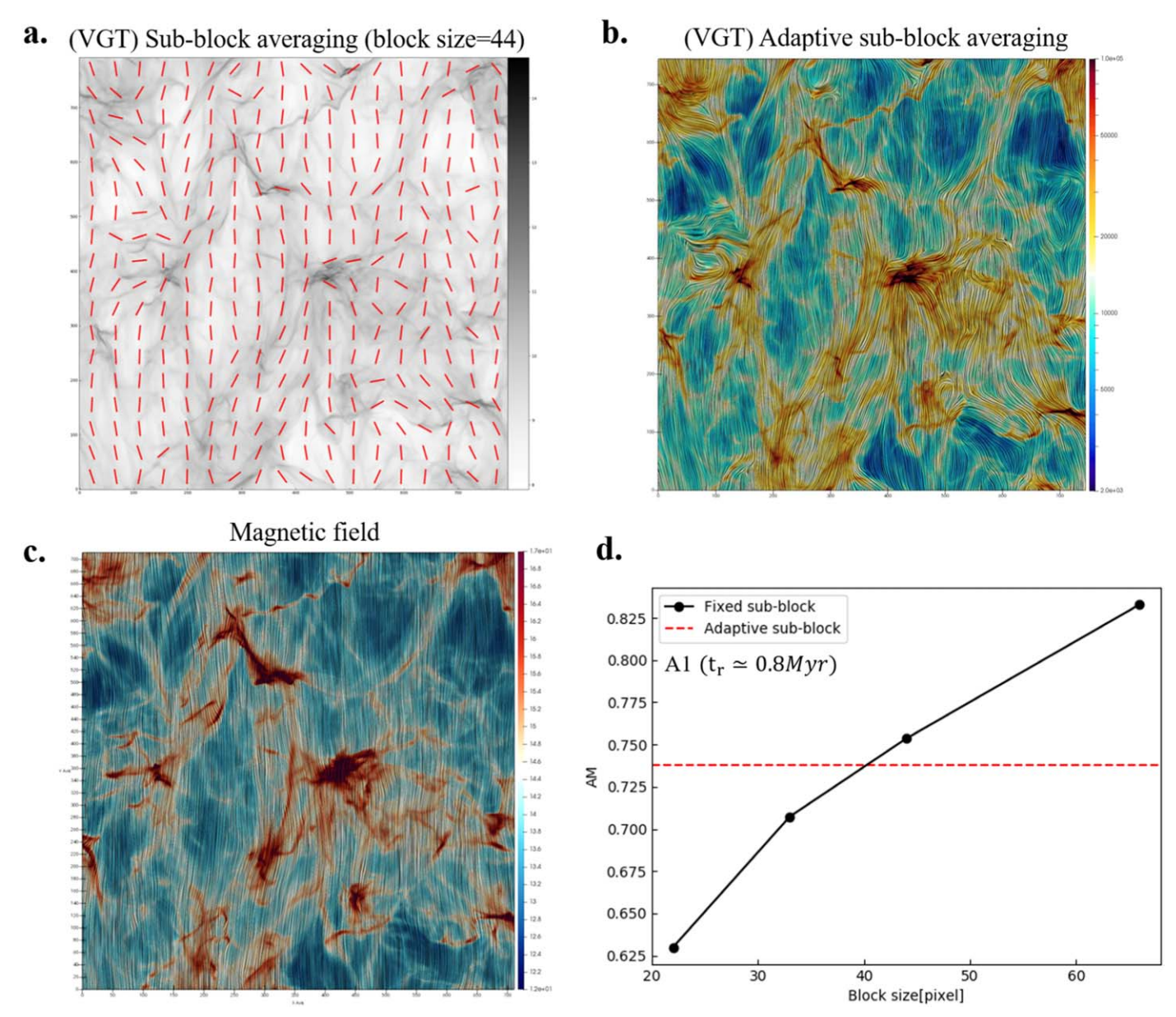


**Figure 6.** Comparison of adaptive sub-block averaging and old sub-block averaging (fixed sub-block size) in terms of the alignment of rotated gradients and magnetic fields. We use the supersonic simulation A1 at  $t_r \simeq 0.8$  Myr. Panel (a): magnetic field (red segments) predicted by VGT with fixed sub-block size 44 pixels. Panel (b): magnetic field (streamlines) predicted by VGT using adaptive sub-block averaging. Panel (c): magnetic field morphology inferred from synthetic polarization. Panel (d): AM of VGT and actual magnetic field in in terms of various fixed block size.

function is defined as:

$$CF(\mathbf{R}) = \langle I(\mathbf{r})I(\mathbf{r} + \mathbf{R})\rangle, \tag{25}$$

where r=(x,y) and R is a lag vector. Figure 8 shows how the correlation function should behave in terms of the contour plot. We can observe that when  $t_r \leq 1.0\,\mathrm{Myr}$ , the contours are elongated along the  $r_\parallel$  direction, i.e., the mean magnetic field direction. As explained in Yuen et al. (2018), the large contours are slightly misaligned from the  $r_\parallel$  direction because of the limited inertial range in numerical simulations. In terms of correlation and structure functions, only the small-scale contributions are considered to be meaningful. Importantly, with the increment of evolution time, the contours change its orientation, becoming elongated along the  $r_\perp$  direction, i.e., perpendicular to the mean magnetic field. We also observed

that the elongation along  $r_{\perp}$  becomes more significant after  $t_r \geqslant 2.6$  Myr, i.e., the ratio of  $\frac{r_{\parallel}}{r_{\perp}}$  decreases. According to our theoretical considerations, in the case of a strong magnetic field, the convergent flow can only have motion along the magnetic field line. Therefore, initially, the turbulent eddies are anisotropic in the direction parallel to the magnetic field, as described in Lazarian & Vishniac (1999). After the self-gravity starts controlling the cloud, the collapsing material converges along the magnetic field direction. The material in the gravitational center, hence, is accumulated as filamentary structures perpendicular to the magnetic field, i.e., elongating perpendicular to the magnetic field.

Crutcher et al. (2010) showed that, in molecular gas, there is a power-law relation between the value of LOS component of magnetic field strength  $B_{los}$  inferred from Zeeman splitting and

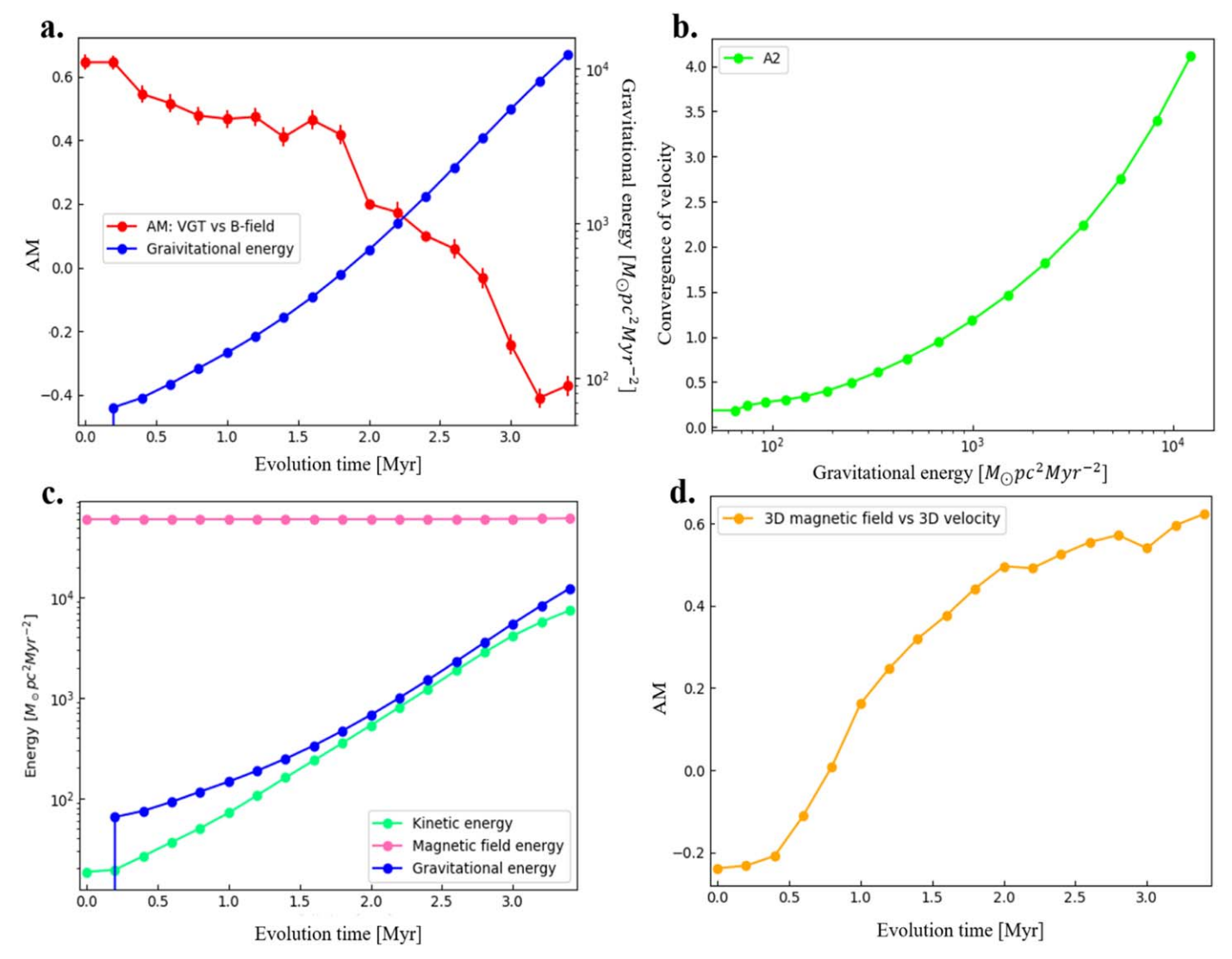


**Figure 7.** Panel (a): AM (red line) between magnetic fields and velocity gradients concerning the time since self-gravity is turned on (0 Myr), using the subsonic A2 simulation set. Blue line indicates the total gravitational energy in each cube. Panel (b): correlation of total gravitational energy and the mean convergence of the 3D velocity field, using subsonic A2 simulations. Panel (c): variation of total kinetic energy, magnetic field energy, and gravitational energy for A2 simulations. Panel (d): AM of the 3D magnetic field angle and 3D velocity angle for A2 simulations.

the volume density n as  $B_{\rm los} \propto n^{0.65}$ . Later, Li et al. (2015) numerically demonstrated that this power law also holds for the total magnetic field strength  $B_{\rm tot} \propto n^{0.62\pm0.11}$ . Similarly, for simulation A2 at  $t_r \simeq 3.4$  Myr, we bin the volume density in uniformly spaced bins with bin size 100 and take the averaged total magnetic field strength within each corresponding bin. Note the difference from Figure 7—the magnetic field used here is the local value instead of the global summation. Due to the finite rate of reconnection, the local magnetic field will be bent, and its strength can increase in the vicinity of the gravitational collapse. In Figure 9, we plot the correlation between the volume density and magnetic field strength. We can see that the density tends to increase with the increment of the magnetic field. At high density range  $n \geqslant 5 \times 10^4$ , there is a power-law relation  $B_{\rm tot} \propto n^{0.60\pm0.03}$ . Summing up the results from Figures 7–9, we can thus conclude that star formation can be efficient in strongly magnetized and fully ionized media.

As above, the convergence of velocity is a proper probe of gravitational collapse. We can thus study the behavior of velocity gradients in collapsing regions using the convergence  $\mathfrak C$ . We plot the 2D histogram of velocity gradients' orientation and the projected velocity's convergence using simulation A2 in Figure 10(a) and (b). At the snapshot  $t_r \simeq 0.0$  Myr, we see that the velocity gradients' orientation is concentrated in the vicinity of  $\pi/2$ . However, at  $t_r = 3.4$  Myr, we see an extreme increment of the convergence. More importantly, the velocity gradients flip their direction by  $\pi/2$ , becoming 0 or  $\pi$ . The whole fraction of the gradients in the range of [0: 0.4] and [2.74: 3.14] is 63.5% of the total volume (summation of all gradients). For some gradients, the change is less than 90°. The reason is presented in Section 5.5; there should be enough self-gravitating gases along LOS to see this change. Therefore, this confirms that velocity gradients change orientation by 90° in the presence of gravitational collapse.

The change of velocity gradients' orientation provides the potential to identify the gravitational collapsing regions without the assistance of polarimetry. For example, as shown in Figure 4, the histogram of velocity gradients' orientation along the boundary of the collapsing region appears as a double-peak feature. The corresponding angular difference between the two

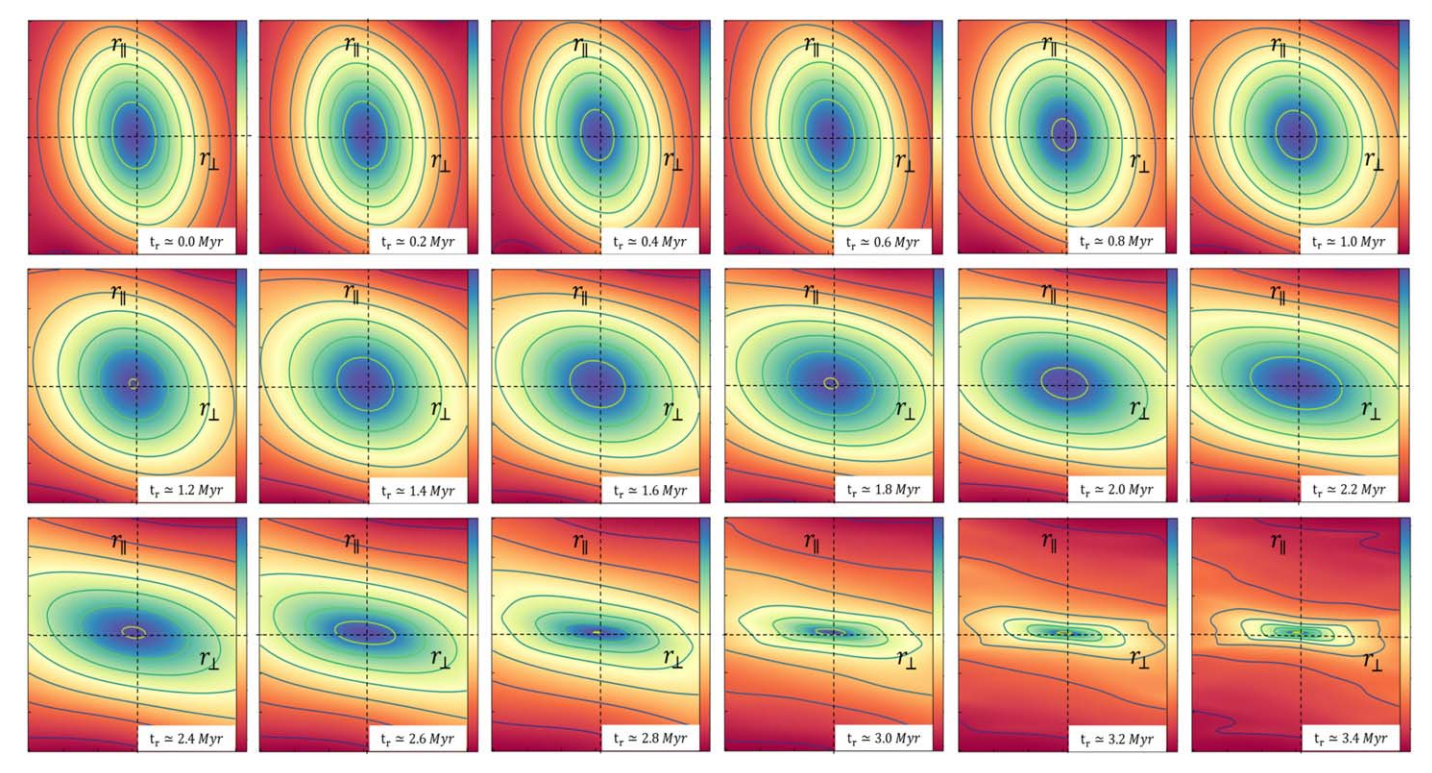
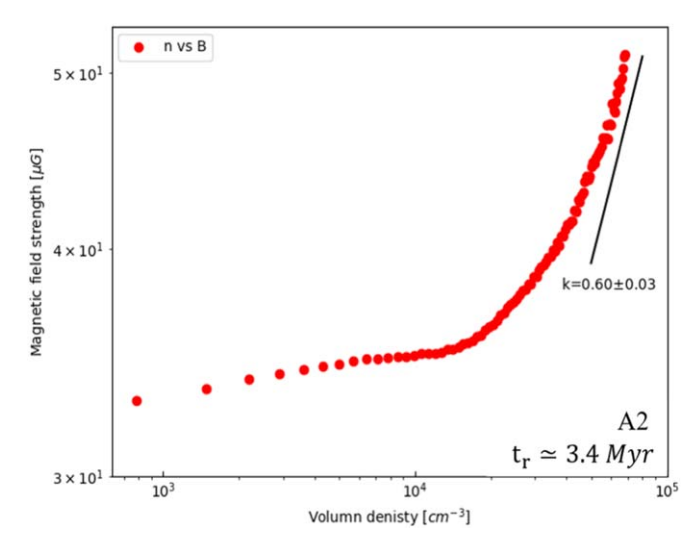


Figure 8. Correlation function of 2D intensity maps at different snapshots, using simulation set A2. Here,  $r_{\perp}$  and  $r_{\parallel}$  are the real space scales perpendicular and parallel to the magnetic field respectively. For all plots,  $r_{\perp}$  and  $r_{\parallel}$  are in scales less than 60 pixels.



**Figure 9.** Correlation of averaged volume density n in uniformly spaced bins and 3D magnetic field strength B using A2 simulation at  $t_r \simeq 3.4$  Myr. Here, k is the slope of the fitted line.

peaks is 90°. This double-peak feature can, therefore, be used to distinguish diffuse and gravitational collapsing regions (see Section 5.6.1). The curvature of velocity gradients will also reach its maximum value on the boundary of the collapsing region, since the gradients rapidly flip their direction by 90° (see Section 5.6.2). There are several ways to detect this change. For instance, one can take calculate the gradient of the resultant velocity gradients' map again, i.e.,  $\nabla(\nabla v(x, y))$ . The amplitude  $|\nabla(\nabla v(x, y))|$  will reach its maximum on the boundary of the collapsing region. Also, we can perform the extrapolation along the direction of velocity gradients in diffuse regions. Because the rotated velocity gradients in the

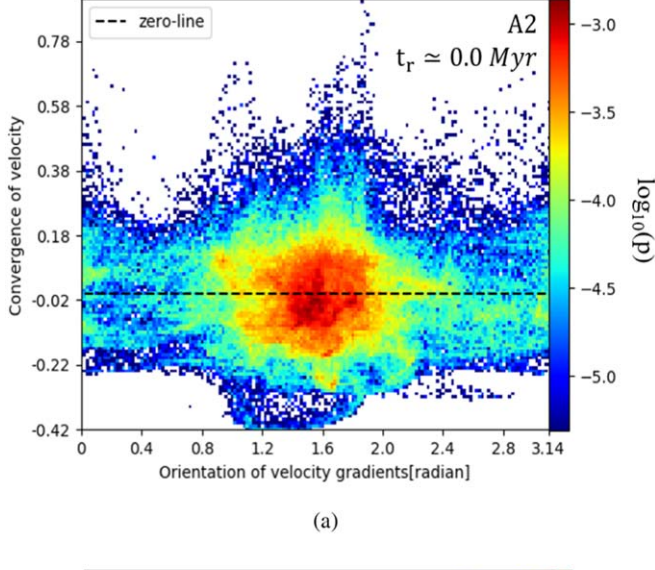
diffuse region are following magnetic field lines, the extrapolated gradients in the collapsing region do not flip their direction. When the difference between the extrapolated gradients and the actual gradient is 90°, we can locate the collapsing region.

# 5.4. The Change of Velocity Gradients' Amplitude

In addition to velocity gradients' orientation, the self-gravity also affects velocity gradients' amplitude. Self-gravitating gas induces an additional force and acceleration to turbulent plasma. As a result, the gradients' amplitude is expected to increase in the gravitationally collapsing region. As shown in Yuen & Lazarian (2018), the dispersion of gradients' amplitude is positively proportional to the evolution time. Therefore, we expect that the analysis of velocity gradients' amplitude can also provide a distinguishable feature in self-gravitating regions.

In Figure 11, we describe the response of velocity gradients' amplitude in the presence of self-gravity. We plot two 2D histograms of logged velocity gradients' amplitude and the projected velocity's convergence using simulation A2 at  $t_r \simeq 0.0$  Myr and  $t_r \simeq 3.4$  Myr, respectively. When the self-gravity is absent, we see the 2D histogram give no preferential direction, i.e., the probability of obtaining large gradients' amplitude is similar for both high-convergence and low-convergence cases. However, the situation is changed when gravitational collapse starts. At  $t_r \simeq 3.4$  Myr, we find that the 2D histogram becomes anisotropic. The high convergence corresponds to only large gradients' amplitude, and low convergence corresponds to small gradients' amplitude. Since

 $<sup>\</sup>overline{^{6}}$  Note that we are using velocity centroid map C(x, y) for the calculation of the normalized velocity gradients' amplitude here. The PCA technique employs the pseudo-Stokes parameters, thus erasing the information of gradients' amplitude.



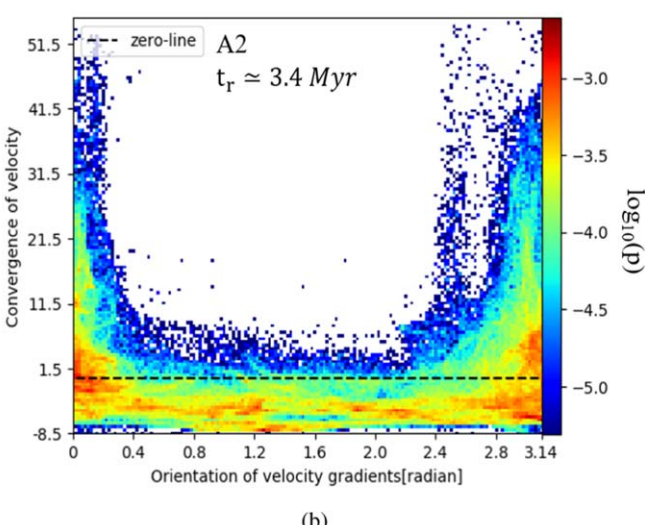


**Figure 10.** Panel (a): 2D histogram of velocity gradients' orientation and velocity's convergence using A2 simulation at  $t_r \simeq 0.0$  Myr. Here, p gives the volume fraction of each data point. Panel (b): 2D histogram of velocity gradients' orientation and projected velocity's convergence using simulation A2 at  $t_r \simeq 3.4$  Myr. Here, p gives the volume fraction of each data point and bin size is 200 for the 2D histograms. Note that the orientation is measured in typical Cartesian coordinate, i.e., with respect to the right horizontal direction.

the high-velocity convergence is induced by self-gravity, large gradients' amplitude is, therefore, the reaction to self-gravity also. It thus provides an alternative way to identify gravitationally collapsing regions through gradients' amplitude.

# 5.5. The Fraction of Collapsing Gas

The velocity gradient exhibits different reactions to the dominance of either turbulence or self-gravity. However, in the 2D map, the particular properties of gradients' change due to self-gravity can only be seen when the fraction of self-gravitating material is sufficiently large. In the case that the fraction of collapsing gas occupies a small volume of the clouds, the projection of both self-gravitating and non-self-gravitating gases can overwhelm the gravitational collapsing region in 2D. For example, in Figure 7, we see that AM, which quantifies the relative orientation between the velocity gradient and magnetic field, is gradually decreasing to negative values.

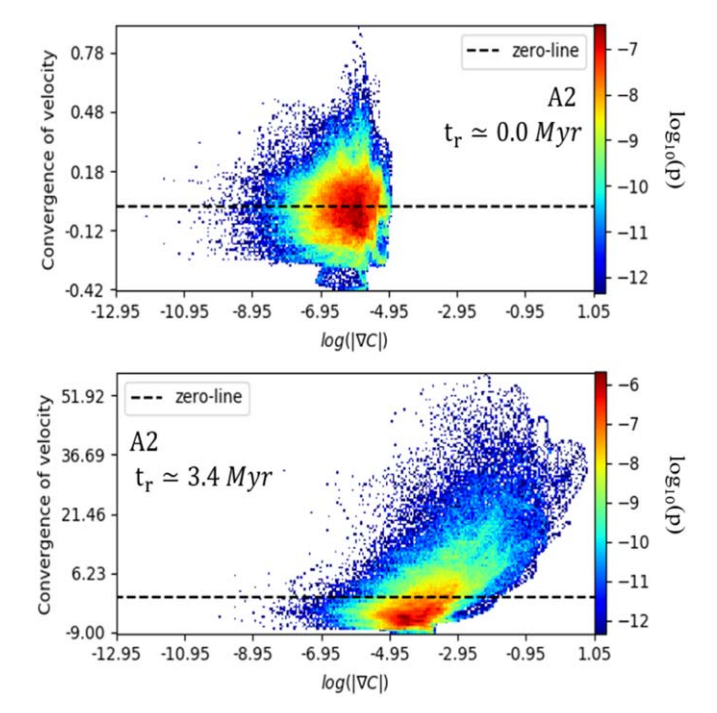


**Figure 11.** Two-dimensional histogram of velocity gradients' amplitude, i.e.,  $\log(|\nabla C|)$ , and velocity's convergence using simulation A2 at  $t_r \simeq 0.0$  Myr (top) and  $t_r \simeq 3.4$  Myr (bottom). Here, p gives the volume fraction of each data point. Bin size is 200 for the 2D histograms.

At the same time, the fraction of collapsing gas is gradually increasing. The negative AM is therefore contributed by more collapsing regions being resolved by VGT.

To test the effect of a small fraction of collapsing gas, we produce a synthetic PPV cube from the MHD simulation A1 at  $t_r = 0.8$  Myr, using a unity density field while keeping the original velocity field unchanged  $M_S = 6.52$ . The unity density field erases all self-gravitating gas. In Figure 12, we plot the actual magnetic field inferred from synthetic dust polarization and also the magnetic fields inferred from VGT (see Section 3). We can see that the magnetic field orientation is distributed around  $\pi/2$  (with respect to the right horizontal direction) and VGT gives a good agreement with the actual magnetic field, i.e., AM = 0.98. The magnetic fields orientation inferred VGT using the actual density field is plotted in Figure 4, showing AM = 0.73. Therefore, it confirms that when most of the matter along the line of sight is not collapsing, VGT does well at tracing the magnetic field, compared with dust polarization.

# 5.6. Identify Gravitational Collapsing Regions through Velocity Gradient

# 5.6.1. Double-peak Histogram of Velocity Gradients' Orientation

As above, we confirm that velocity gradients change orientation by  $90^{\circ}$  in the presence of the gravitational collapse (see Section 5.3). We thus expect, when getting close to the boundary of self-gravitating gas, that the histogram of gradients' orientation will appear as a double-peak feature (see Figure 4). The algorithm of the double-peak feature is therefore used to locate gravitating collapsing gas (see Section 3.2 for details).

In Figure 13, we zoom in on two subregions, A1-1 and A1-2, from simulation A1 at  $t_r \simeq 0.8$  Myr. These subregions both contain well-defined convergent flows. We plot the gradients'

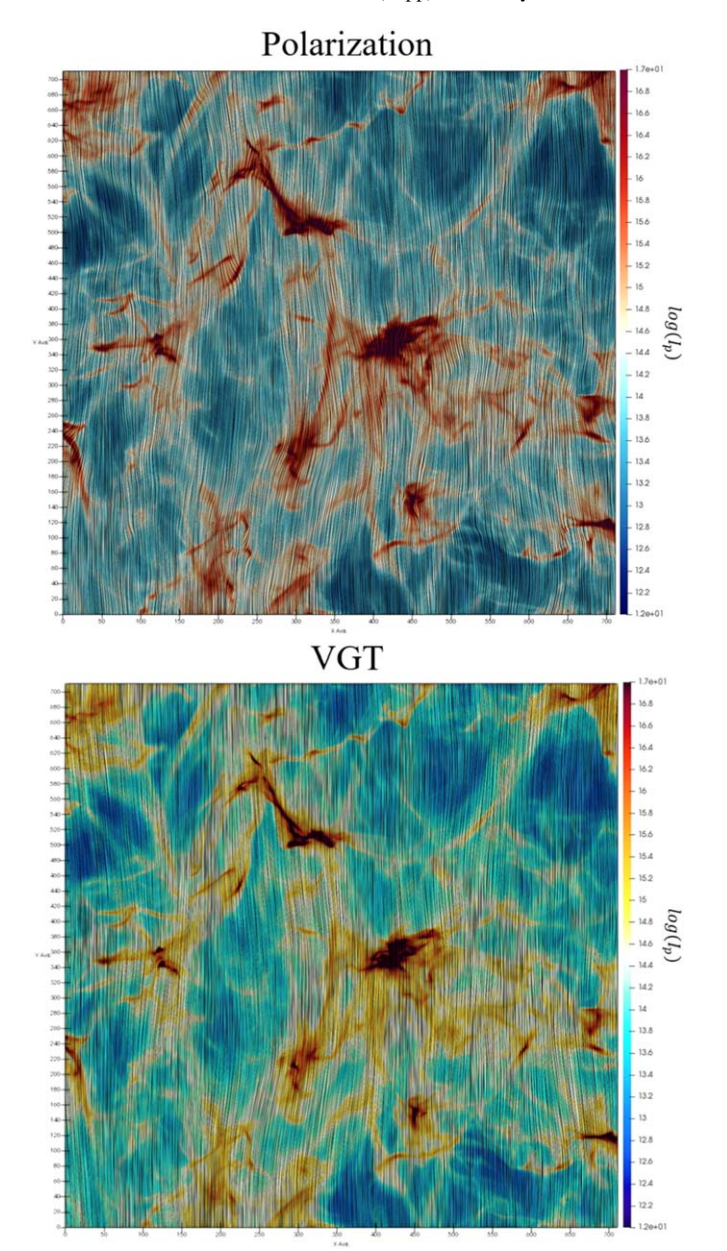


**Figure 12.** Magnetic field derived from polarization (top) and magnetic field inferred from VGT (bottom) using a synthetic PPV cube. Magnetic field is superimposed on the polarized intensity map  $I_p$  and visualized using the LIC. Cube is produced from MHD simulation A1 at  $t_r = 0.8$  Myr, using a unity density field while keeping the original velocity field unchanged  $M_S = 6.52$ , i.e., all collapsing materials are removed. Corresponding AM = 0.98.

orientation and the velocity convergence projected from 3D for each region. We see that some gradients flip their directions by  $\pi/2$ . These resulting gradients are either 0 or  $\pi$ . One possible explanation is the different directions of infall gas. We compare the change of gradients' orientation with the N-PDF method (see Figure 13). First of all, we observe that the majority of self-gravitating regions identified from the two methods are similar and reflect the convergent flows. However, for the A1-1 region, we find there exists a filamentary structure that is identified as self-gravitating by N-PDFs but not by the double-peak algorithm. For N-PDFs, it gives a density threshold to distinguish high-density gas showing self-similarity. However, the high-density gas contains not only self-gravitating materials but probably also non-self-gravitating density enhancement. As

a result, the PDF method could mix self-gravitating structures and non-self-gravitating density enhancement. The second reason could come from velocity gradients. In Figure 7, velocity gradients hold their orientation with little change at the early stages of collapsing. We can expect that the velocity field is significantly changed only when the gravitational energy dominates over the kinematic energy of turbulence. In this case, this filamentary structure could be at the beginning of collapse. Also, if the collapsing fluid occupies only a small volume along LOS, the change of velocity gradients can be insignificant (see Section 5.5).

For the implementation of the double-peak algorithm, we first produce a pixelized map of velocity gradients' orientation using the adaptive sub-block averaging method (see Figure 13(a)). Based on the resultant velocity gradients' map after the adaptive sub-block, we draw the histogram of gradient orientation again in another sub-block (which it is denoted as the second sub-block) and recognize the features of a double peak based on the orientation distribution after the adaptive sub-block. Note that the second sub-block here is different from the one for the first step of magnetic fields tracing (see Section 3.2). Since the second sub-block does not require a Gaussian fitting, we do not utilize an adaptive sub-block size, but instead keep it fixed (see Section 3.2 for details). In Figure 13, we vary the size of the second block and highlight the entire region enclosed by the boundary identified by the double peak using the color red. We can see that a large block size of 50 produces a more significant boundary of the selfgravitating region, which is expected. We compare velocity's mean convergence in the self-gravitating regions identified from N-PDFs and VGT's double-peak algorithm, as well as the global mean convergence in the entire subregion (see Figure 14). For VGT with the double-peak recognition algorithm, the convergence is not constant. A large second block, as well as the procedure of adaptive sub-block averaging, would include more noncollapsing gas so that the convergence becomes small. Both the adaptive sub-block averaging method and the double-peak algorithm would include additional parts of nonconvergent material, due to the blocks on the boundary. This explains why the convergence obtained from the PDF method is always larger. To have the best performance, the block size should be selected until the histogram shows two apparent Gaussian distributions. In addition, in both of these regions, we can see that the convergences for VGT are positive and more significant than their corresponding global mean convergences.

# 5.6.2. The Curvature of Velocity Gradients

The curvature of velocity gradients reaches its maximum value when the gradients flip their direction by 90°, but the ambient region usually has small curvature. The curvature therefore provides a second way to identify the self-gravitating regions by sorting out the curvatures. In Figure 15, we give an example of how the curvature algorithm works. We use three different collapsing stages of the subregion A1-2, i.e., 0.4, 0.6, and 0.8 Myr. At the initial stage of collapse, we expect that there exists a large amount of convergent gas, and the dynamics become slim at the later collapsing stage. This can be measured from the changes in gradients' orientation. Figure 15 shows that the area in which gradients change directions decreases in size when the evolution time goes up. It is clear that the red tail in this area is vanishing. In the second row of Figure 15, one

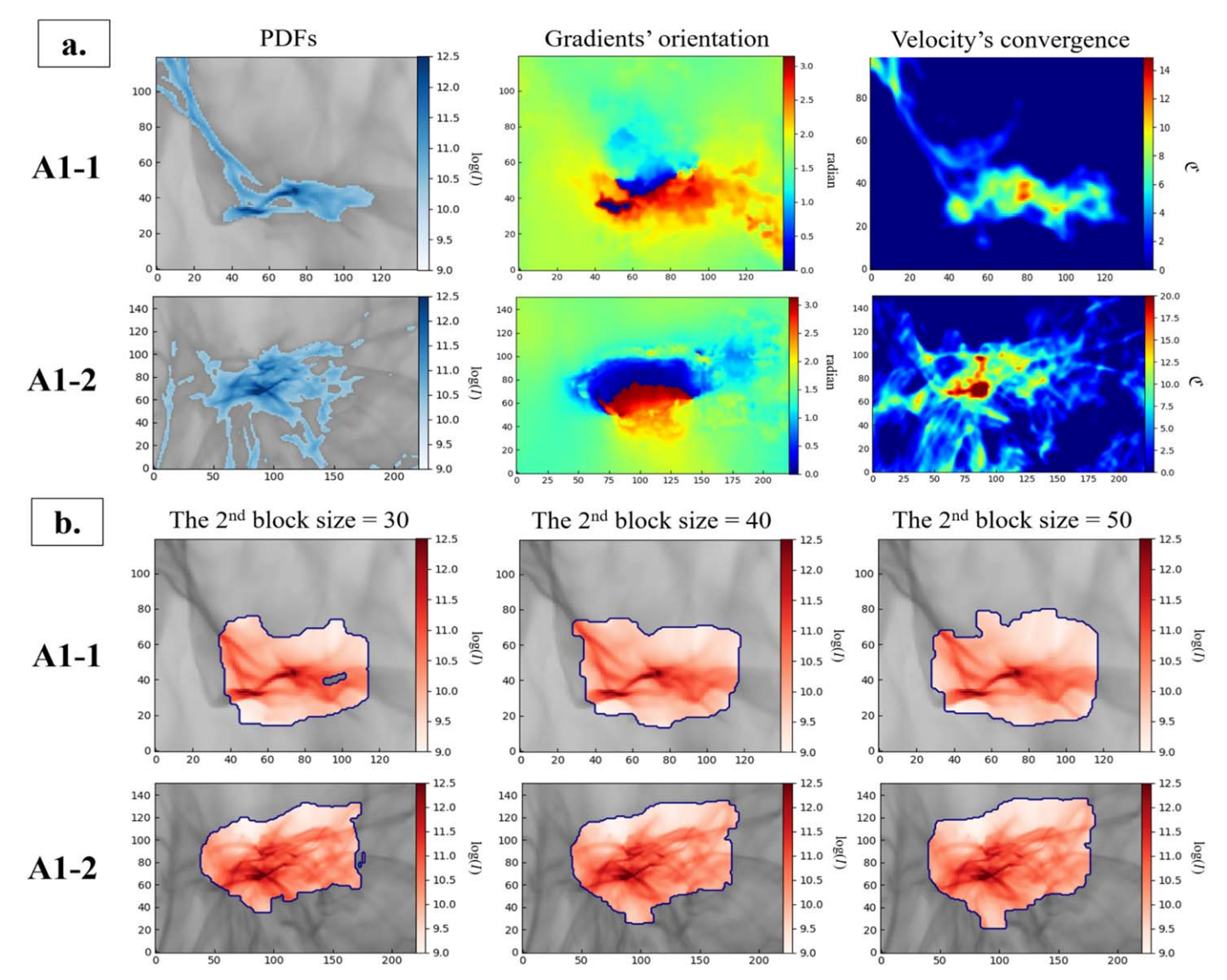


Figure 13. Panel (a): the first and second rows are two subregions extracted from simulation A1 at  $t_r \simeq 0.8$  Myr, denoted as A1-1 (length scale  $\simeq 1.7$  pc) and A1-2 (length scale  $\simeq 2.8$  pc), respectively. First column: gravitationally collapsing regions (blue regions) identified from the N-PDFs. Second column: orientation of velocity gradients in the range of  $[0, \pi]$  (i.e., red:  $\simeq \pi$ , blue:  $\simeq 0$ , and green:  $\simeq \pi/2$ ). Third column: projected velocity convergence of each corresponding region. Discontinuity comes from numerical effect. Panel (b): gravitationally collapsing regions (red regions) identified from the double-peak feature of velocity gradients' morphology. Second block size is implemented in the double-peak algorithm to plot the histogram of velocity gradients' orientation in a subregion. We test three block sizes: 30, 40, and 50 pixels.

can see that the gradients' curvature becomes significantly larger at the boundary of collapsing regions. However, the curvature does not reveal the region where the change of velocity gradients' direction is less than 90°. For example, when the collapsing material only occupies a small fraction of the cloud along the LOS, the resulting gradient can have a change of direction less than 90°. We expect this is the reason we see three disconnected self-gravitating regions in the third row, 0.4 Myr, of Figure 15. According to the enclosed boundary outlined by the curvature, we figure out the full collapsing regions using the "contourf" function of Julia (Bezanson et al. 2012). One can see the formation of the core at  $t_r = 0.8 \,\mathrm{Myr}$ , and the collapsing region is shrinking in size. Compared with the collapsing regions identified from N-PDFs (see Figure 15, fourth row), we get similar results for both VGT and N-PDFs methods at  $t_r = 0.8 \,\mathrm{Myr}$ . However, N-PDFs indicate a smaller collapsing area than does VGT at  $t_r = 0.4 \,\mathrm{Myr}$  and  $t_r = 0.6 \,\mathrm{Myr}$ . One reason is that N-PDFs

do not measure the existence of the continuous inflow into the star-forming cores at the early stages of star formation, before enough gas is accumulated in the core, but VGT samples velocities and therefore it is sensitive to the inflow.

We show in Figure 10 that the large convergence in collapsing regions guarantees a large amplitude of velocity gradients. Therefore, we study the gradient amplitude in the collapsing region identified from VGT and N-PDFs. In Figure 16, we calculate the average value of gradients' amplitude in the corresponding collapsing regions and also the global mean value of the amplitude. We can see that both VGT and N-PDFs always give the gradients amplitudes more significant than the global mean value. However, in some cases, N-PDFs can also show a higher amplitude than does VGT. The adaptive sub-block averaging method still contributes to the difference, as does the second sub-block, because the utilization of both sub-blocks will take into account extra nonconvergent inflow. However, the sub-block averaging is not

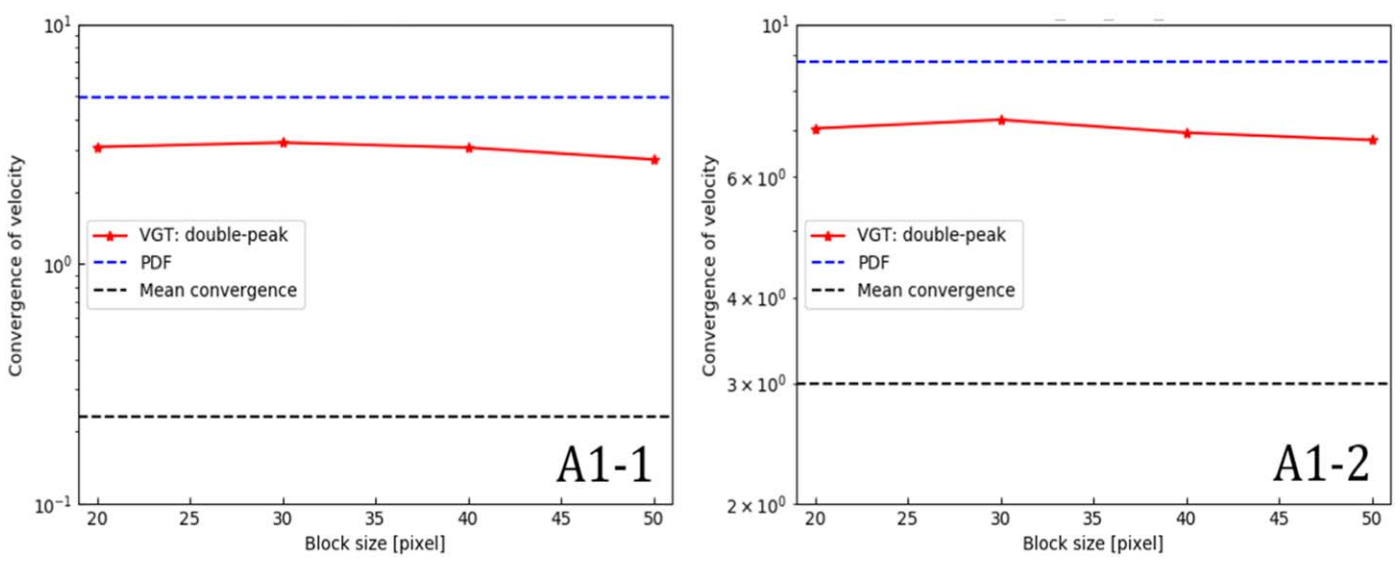


Figure 14. Comparison of velocity's mean convergence in the self-gravitating regions identified from N-PDFs (blue dashed line) and VGT's double-peak algorithm (red solid line). The two corresponding regions are shown in Figure 15. Black dashed line indicates the global mean convergence in each region.

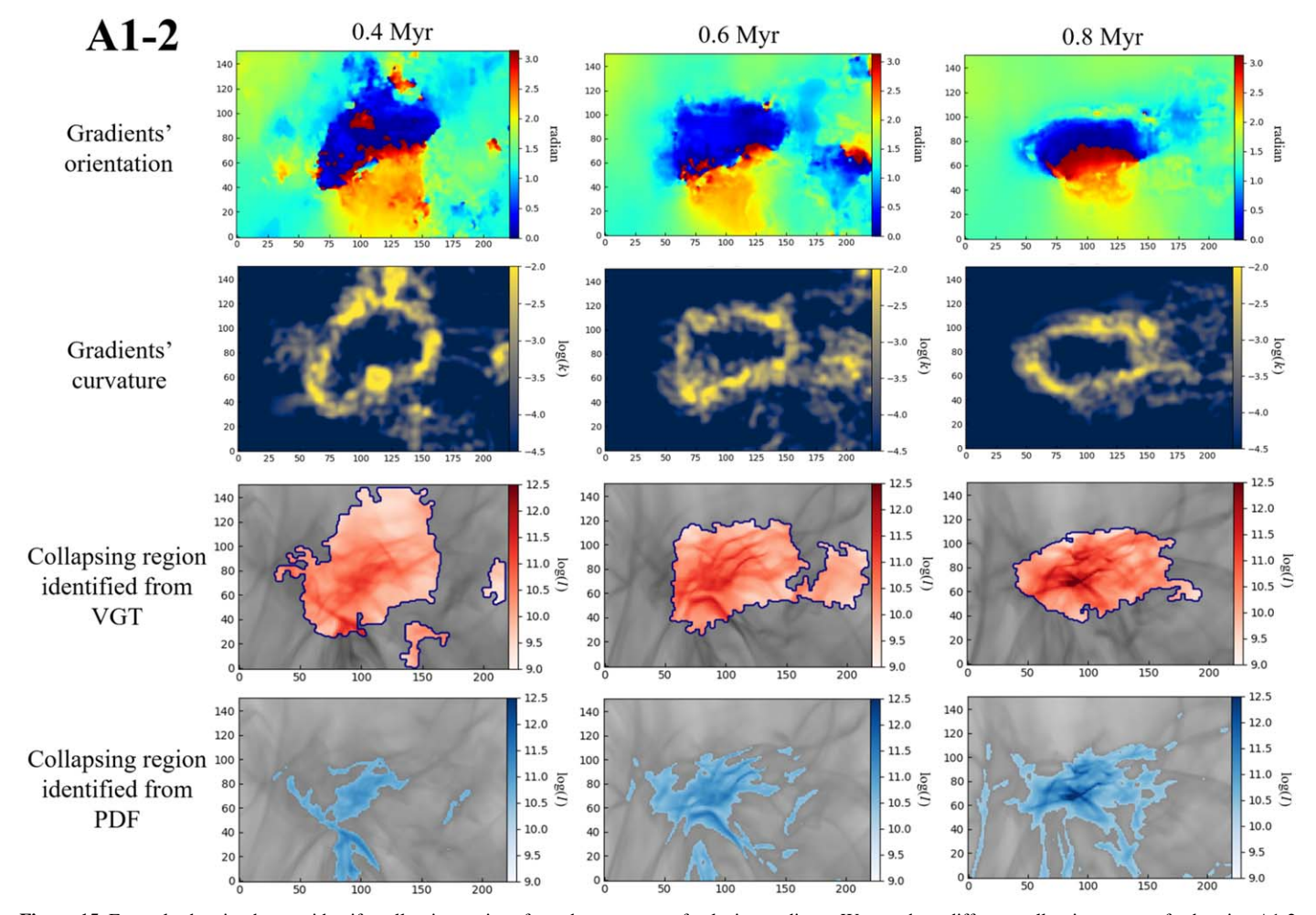
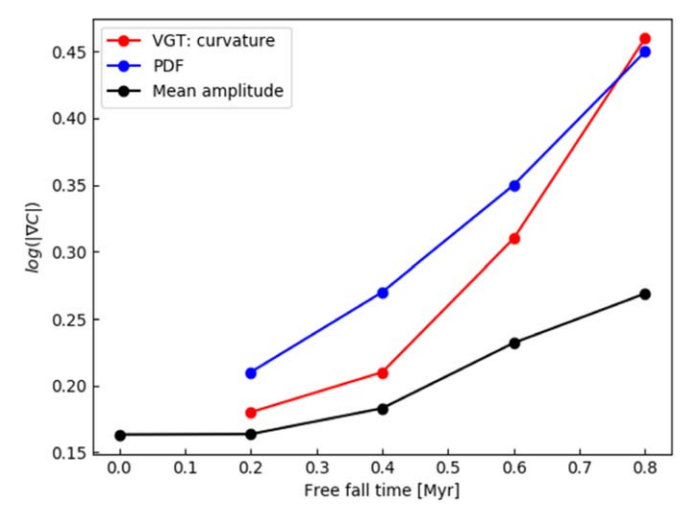


Figure 15. Example showing how to identify collapsing regions from the curvature of velocity gradients. We use three different collapsing stages of subregion A1-2, i.e., 0.4 Myr (first column), 0.6 Myr (second column), and 0.8 Myr (third column). First row: orientation of velocity gradients in the range of  $[0, \pi)$  (i.e., red:  $\simeq \pi$ , blue:  $\simeq 0$ , and green:  $\simeq \pi/2$ ). Second row: curvature of velocity gradients calculated via the RK2 method. Third row: gravitationally collapsing regions (red regions) identified from the curvature of velocity gradients. Fourth row: gravitationally collapsing regions (blue regions) identified from the N-PDFs.



**Figure 16.** Comparison of the average velocity gradients' amplitude in the self-gravitating regions identified from N-PDFs (blue) and VGT's curvature algorithm (red). Corresponding regions are shown in Figure 15. Black line indicates the global mean convergence in each region.

implemented in the calculation of gradients' amplitude, and high amplitude is only induced by self-gravity. With the assistance of gradients' amplitude, it is possible to get rid of the extra non-self-gravitating regions introduced by both subblocks.

wIn Figure 17(a), we outline the areas of gradients' amplitude corresponding to the collapsing regions identified by VGT (see Figure 15), but at different collapsing stages  $t_r \simeq 0.4$ , 0.6, and 0.8 Myr. In the same regions, we also mask the low-amplitude pixel, i.e., its corresponding amplitude is less than the global mean value. The remaining areas, therefore, have high-amplitude gradients and high convergence, i.e., the convergent inflow. We can see in Figure 17 that the inflow is slight but covers a larger area at  $t_r = 0.4$  Myr. At  $t_r = 0.6$  Myr, the inflow gets stronger and finally goes into the core of star formation at  $t_r = 0.8$  Myr. In Figure 17(b), we plot the actual 2D convergent flow map (i.e., the density structures correspond to positive convergence) normalized by the total column density along the particular line of sight. Comparing with the actual convergent flow, we can see both N-PDF and VGT give similar answers and can determine the projected convergent flow by themselves. Note that, at  $t_r = 0.4 \,\mathrm{Myr}$  and  $t_r = 0.6 \,\mathrm{Myr}$ , the convergent flow obtained from VGT occupies an area larger than the one defined by the N-PDFs (see Figure 15). We expect the reason is that N-PDFs are sensitive only to the already formed accreting cores, but gradients trace the entire convergent flow. The outcome of VGT is also affected by the fraction of collapsing gas in the cube. In Section 5.5, we show that when most of the matter along the line of sight is not collapsing, VGT may not reveal the collapsing region. As for the N-PDFs, in addition to the issue of the low fraction of collapsing gas, the low-density part of collapsing gas may also be overwhelmed because of the projection effect. To justify this point, we show the 3D visualization of actual convergent flow at  $t_r = 0.6$  Myr in Figure 17(c) and (d). We use a blue box to outline the corresponding 3D convergence identified by VGT and N-PDFs, respectively. We can see the convergent area defined by VGT include the majority of 3D convergent flows, while the N-PDFs give only the strongly convergent fluid, which does not cover the convergence on the top volume. We find the convergent fluid on the top corresponds

to the low-intensity region of the 2D projected intensity map (see Figure 17(d)). The N-PDFs, therefore, do not resolve the low-intensity part because the transition threshold  $S_t$  of N-PDFs only highlights the high-intensity part (see Section 2). As for the bottom part of the 3D convergence, the fraction of collapsing gas is minimal (see Figure 17(d)). Its 2D projection is therefore dominated by noncollapsing gas.

In addition, we calculate the mean convergence for the regions corresponding to: (i) the inflow outlined by the VGT (curvature and amplitude algorithm), (ii) the collapsing region identified by the curvature algorithm, (iii) the collapsing region identified by N-PDFs, and (iv) the entire A1-2 region. The result is presented in Figure 18. First, we see that the global mean convergence is increasing with the evolution of gravitational collapsing. Both VGT and N-PDFs always give larger convergence than the global mean value, while N-PDFs can also show a larger convergence than VGT employing only the curvature algorithm. In particular, at  $t_r = 0.4$  Myr and  $t_r = 0.6$  Myr, VGT (curvature and amplitude) appears to have a larger range of inflow and the largest convergence. As for the very initial and final moments, i.e.,  $t_r = 0.2 \,\mathrm{Myr}$  and  $t_r = 0.8 \,\mathrm{Myr}$ , the dynamics of collapse are less significant, and the VGT (curvature and amplitude) includes some nonconvergent fluid. The performance of VGT in identifying gravitational collapsing region is therefore comparable or better to the N-PDFs.

# 6. Identifying Gravitational Collapsing Regions with Intensity Gradients

It has been shown that intensity gradients also change their direction by  $90^{\circ}$  in the presence of gravitational collapse (Yuen & Lazarian 2017b; Hu et al. 2019a). Here, we apply the tools developed in this paper, i.e., the adaptive sub-block averaging and curvature algorithm, to identify the gravitationally collapsing region using the IGT. The intensity map I(x, y) is produced through the integration of PPV cubes along the line of sight:

$$I(x, y) = \int \rho(x, y, v) dv,$$
 (26)

where  $\rho$  is gas density and v is the velocity component along the line of sight. By means of convolution with Sobel kernels  $G_x$  and  $G_y$ , we obtain the intensity gradient orientation at individual pixel (x, y):

$$\nabla_{x}I(x, y) = G_{x} * I(x, y)$$

$$\nabla_{y}I(x, y) = G_{y} * I(x, y)$$

$$\psi(x, y) = ASB \left[ tan^{-1} \left( \frac{\nabla_{y}I(x, y)}{\nabla_{x}I(x, y)} \right) \right], \tag{27}$$

where  $\nabla_x I(x, y)$  and  $\nabla_y I(x, y)$  are the *x* and *y* components of the intensity gradients, respectively. ASB denotes the implementation of the adaptive sub-block averaging method (see Section 5.2), and  $\psi$  is the resultant intensity gradient map.

As an analogy to the velocity gradient, we repeat the same analysis for the intensity gradient in order to study its properties in collapsing regions. In Figure 19, we plot the 2D histograms of the intensity gradients' amplitude, i.e.,  $\log(|\nabla I|)$ , and velocity's convergence using the A2 simulation at  $t_r \simeq 0.0$  Myr and  $t_r \simeq 3.4$  Myr. In the absence of self-gravity, i.e., at  $t_r \simeq 0.0$  Myr, the convergence of velocity is low and the histogram slightly deviates toward the part where gradients

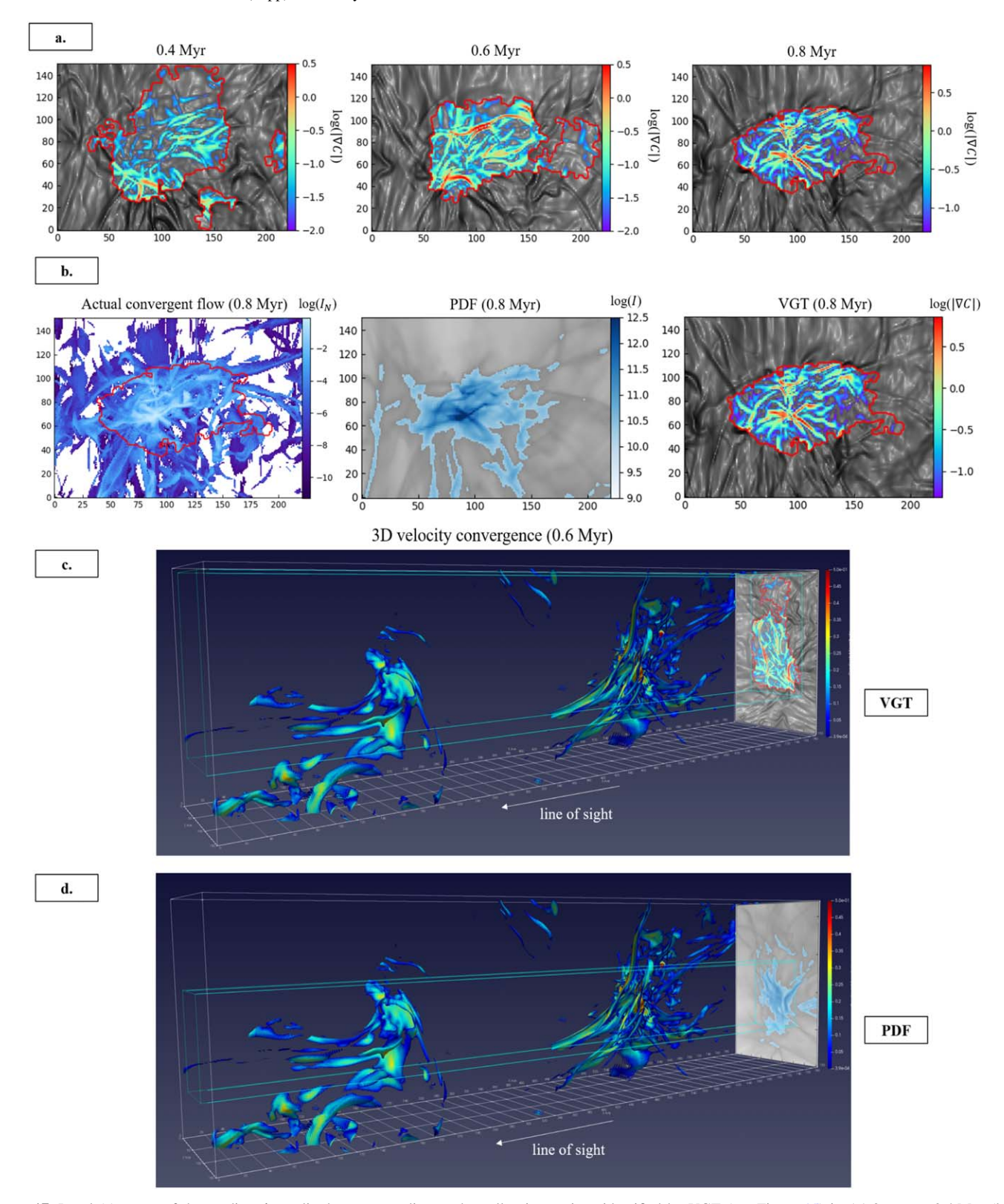
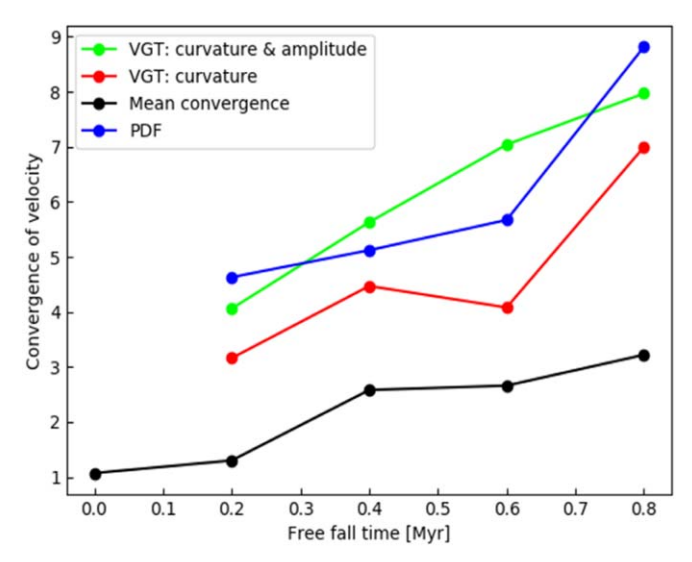


Figure 17. Panel (a): areas of the gradients' amplitude corresponding to the collapsing regions identified by VGT (see Figure 15) in A1-2 at  $t_r \simeq 0.4$  Myr (left), 0.6 Myr (middle), and 0.8 Myr (right). In the same regions, we mask the low-amplitude pixel, i.e., its corresponding amplitude is less than the global mean value. Remaining colorful areas indicate high-amplitude gradients and a high convergence, i.e., the convergent inflow. Panel (b): comparison of the convergent flow determined by the PDF (middle), VGT (right), and the actual convergent flow (left) at  $t_r \simeq 0.8$  Myr. Here,  $I_N$  is the projection of normalized volume density. Panel (c): visualization of 3D velocity convergence. Positive convergence outlines the convergent inflow. Inner blue box approximately outlines the boundary of the collapsing region identified from VGT. Panel (d): visualization of 3D velocity convergence. Inner blue box approximately outlines the boundary of the collapsing region identified from N-PDFs.



**Figure 18.** Comparison of velocity's mean convergence for the regions corresponding to: (i) the inflow outlined by the curvature and amplitude (lime), (ii) the collapsing region identified by the curvature algorithm (red), (iii) the collapsing region identified by N-PDFs (blue), and (iv) the entire A1-2 region (black).

have high-intensity amplitude. In general, the probability of obtaining a high amplitude for the intensity gradients is similar in both high-convergence and low-convergence cases. Figure 10, on the other hand, shows a similar histogram of velocity gradients' amplitude to be more isotropic. When the self-gravity grows strong, i.e., at  $t_r \simeq 3.4 \,\mathrm{Myr}$ , the 2D histogram becomes very anisotropic. The high convergence corresponds to only large gradients' amplitude, and low convergence corresponds to small gradients' amplitude. Since the high-velocity convergence is induced by self-gravity, large gradients' amplitude is, therefore, the outcome of self-gravity. In the bottom row of Figure 19, we give the 2D histograms of intensity gradients' orientation and velocity's convergence still using the A2 simulation at  $t_r \simeq 0.0$  Myr and  $t_r \simeq 3.4$  Myr. We see that the histogram is close to a uniform distribution. For either the positive convergence part or negative convergence part, one is equally able to find the orientation of intensity gradient in the full range of  $[0, \pi)$ . However, the distribution of velocity gradients only concentrates on the  $\pi/2$  (see Figure 7), which is the mean magnetic field direction in our simulation. Velocity gradients are, therefore, more accurate in terms of magnetic field probing than intensity gradients. As for  $t_r \simeq 3.4 \, \mathrm{Myr}$ , the distribution of intensity gradients deviates toward either 0 or  $\pi$ , i.e., gradients become perpendicular to the magnetic field (note we rotate gradients by 90° in this work). Therefore, in the case of gravitational collapse, both velocity gradient and intensity gradient flip their direction by 90°, and large gradients' amplitudes are induced simultaneously. The intensity gradient thus provides an alternative way to identify regions of gravitational collapse.

In Figure 20, we apply the curvature algorithm to identify the collapsing part in subregion A1-2 at  $t_r \simeq 0.4$  Myr, 0.6 Myr, and 0.8 Myr, respectively (see analysis in Figure 15). First, we see intensity gradients change their orientation at the vicinity of the core. However, the area showing the change is significantly larger than the one seen in velocity gradients' orientation, while its evolution is similar. At  $t_r \simeq 0.4$  Myr, the top and bottom parts initially show the change of gradients' direction, but at

 $t_r \simeq 0.8 \, \mathrm{Myr}$ , the change disappears in these two areas. According to our theoretical consideration, both intensity and velocity gradients are sensitive to the motion of infall fluid. Once the collapse has been completed without surrounding infall fluid, the gradients do not distinguish the core. We distinguish the collapsing region and see that some diffuse regions on the right side of the intensity map are also covered. Because the intensity gradients are sensitive to both self-gravity and shock (Hu et al. 2019a), the change in the diffuse area might come from shocks. Recall that self-gravity will also induce a larger amplitude of intensity gradients, but this is not the case for shock, i.e., the upper limit of the amplitude depends on the compressibility  $\beta$  (Yuen & Lazarian 2018; Xu et al. 2019). We then also highlight the high-amplitude part (i.e., its corresponding amplitude is larger than the global mean value) in Figure 20. We see that large gradients' amplitude only appears in the vicinity of the collapsing core, while the diffuse region only shows small values of gradients' amplitude. As for velocity gradients, we show in Figure 18 that they disclose the self-gravitating region.

To justify our consideration of shocks, we give the 3D visualizations of velocity convergence in Figure 21, using simulation A1 at  $t_r \simeq 0.8$  Myr. As with Figure 18, we remove negative convergence to outline the convergent inflow and mask the low-amplitude pixel, i.e., its corresponding amplitude of intensity gradients is less than the global mean value. The largeamplitude region agrees with the high-convergence region. As for the small-amplitude region at the top, the convergence is insignificant and is not expected to be resolved by gradients. In addition, in Figure 21, we outline those high-intensity structures with intensities five times larger than the global mean value. Recall that the magnetic field is pointing toward or away from the viewer (i.e., along the z-axis) in this visualization. We can see that those high-intensity structures are perpendicular to magnetic fields, as explained in Xu et al. (2019). In the bottom panel of Figure 21, we show the 3D visualizations of high gravitational energy, i.e., the corresponding gravitational energy in each pixel is five times larger than the global mean value. As we expected, the upper right volume is not bounded by gravitational energy but is filled with high-intensity structures, which are believed to be shocks. After projection, this shock space matches the area in which the intensity gradients change their orientation. The change of intensity gradients' orientation in the diffuse region is, therefore, mostly coming from the contribution of shocks. We then can distinguish the collapsing regions and shocks through the comparison of intensity gradients' orientation and amplitude, as well as velocity gradients. More importantly, the gravitationally collapsing region identified by VGT agrees with the 2D projection of space with high gravitational energy. Also, in Figure 22, we find in the zoomed-in collapsing region, the local magnetic field energy reaches its maximum at the center of the collapsing clump. Although the turbulent reconnection tries to minimize the increment of the magnetic field, the effect is constrained by its finite rate in high-density regions. We can, therefore, observe a stronger magnetic field in the collapsing center.

Figure 22 also shows that our finding of the gravity-induced convergent flow is converged in terms of resolution. In Figure 7, we use the A2 simulation with a resolution of 480<sup>3</sup>, showing that the magnetic field tends to follow the convergent flow. Figure 22 visualizes this phenomenon using the A1 simulation with a resolution of 792<sup>3</sup>. Indeed, as the gravitational collapse is not bounded, the convergent flow will spread

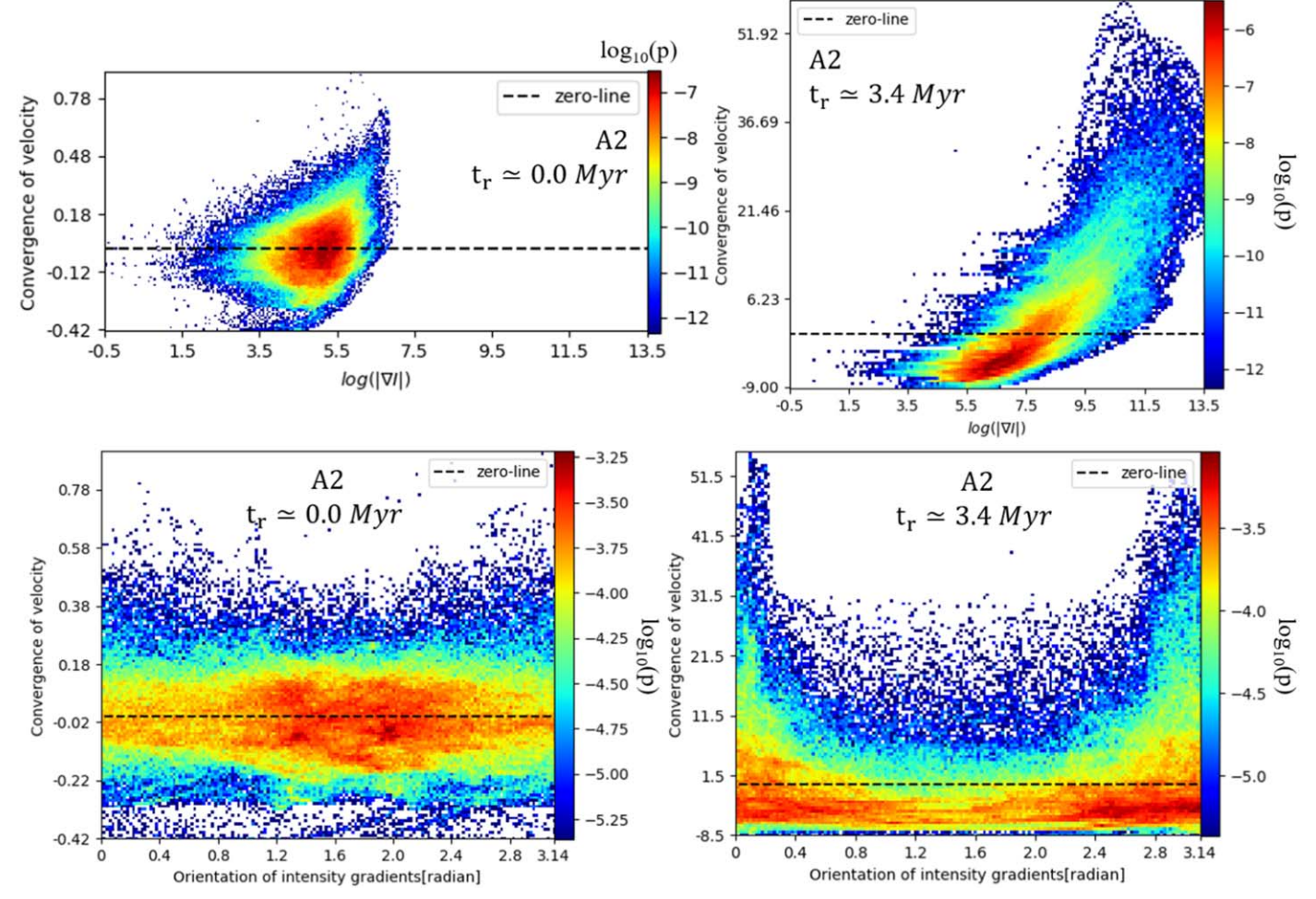


**Figure 19.** Top row: 2D histogram of intensity gradients' amplitude, i.e.,  $\log(|\nabla I|)$ , and velocity's convergence using A2 simulation at  $t_r \simeq 0.0$  Myr (left) and  $t_r \simeq 3.4$  Myr (right). Here, p gives the volume fraction of each data point. Bottom row: 2D histogram of intensity gradients' orientation and velocity's convergence using A2 simulation. Note that the orientation is measured in typical Cartesian coordinates, i.e., with respect to the right horizontal direction. Bin size is 200 for the 2D histograms.

to all surrounding pixels with the increment of evolution time. Otherwise, to see the convergence at the very beginning of the collapse, we need a very high resolution to resolve the collapsing core.

The combination of VGT and IGT can also be used to determine the stages of gravitational collapse. For instance, comparing Figures 20 and 15, we find that the dense collapsing region identified by IGT is still larger than the one identified by VGT. Considering the physical evolution of intensity and velocity fields, the velocity field is dramatically changed only when the gravitational energy dominates over the kinematic energy of turbulence, but the intensity field's change is accumulating. Therefore, the change of intensity gradients would be observed in the initial collapsing stages. As a result, we can determine the collapsing stages through the comparison of VGT and IGT. The first stage is the onset of collapse, during which the rotated velocity gradients and intensity gradients, together with the magnetic field, are aligned with each other. Next, during the middle stage of collapse, the rotated velocity gradients are still parallel to magnetic fields, while the intensity gradients show no alignment with either the velocity gradients or magnetic fields. In the final stage of collapse, the rotated velocity gradients and intensity gradients are antialigned (perpendicular)

to the magnetic field, while velocity gradients and intensity gradients are aligned parallel to each other.

# 7. Discussion

7.1. Identifying Self-gravitating Regions from Velocity Gradients and Intensity Gradients

#### 7.1.1. Implications for Velocity Gradients

The novel VGT technique utilizes the velocity gradient to trace the magnetic field based on the anisotropic properties of MHD turbulence. The properties of turbulence are modified in self-gravitating environments. As shown in Figure 22, in a gravitationally collapsing region with sub-Alfvénic conditions, the magnetic field is strong enough to provide a supporting force. This magnetic force counteracts any gravitational pull inducing the acceleration, which is perpendicular to the magnetic field. The gravitational force, therefore, produces the most significant convergent plasma accelerating in the direction parallel to the magnetic field. The maximum spatial difference of velocity then follows the same direction as the convergent flow, which means the velocity gradients are parallel to the magnetic field. Comparing with the non-self-gravitating turbulence, in which the velocity gradients are

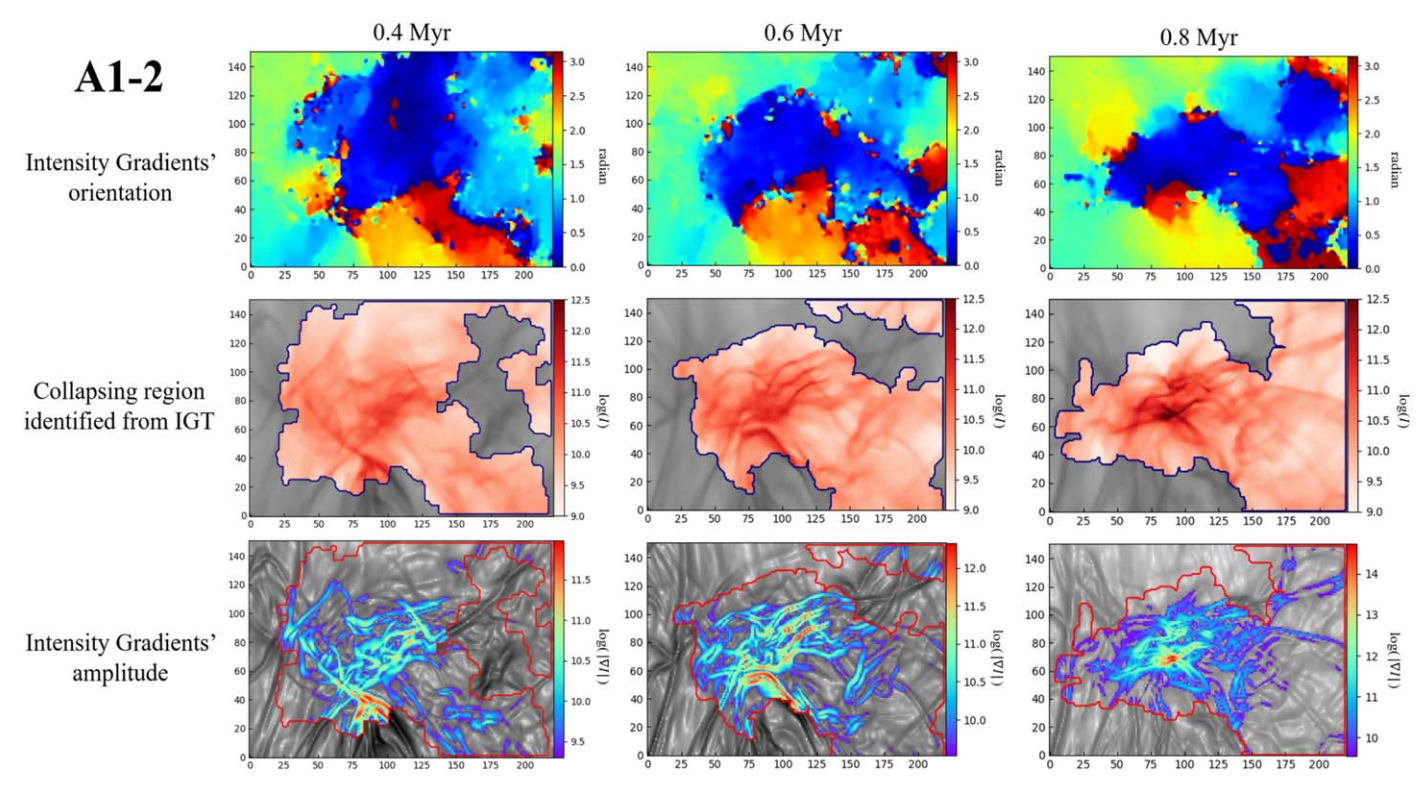


Figure 20. Example showing how to identify collapsing regions from the curvature of intensity gradients. We use three different collapsing stages of subregion A1-2, i.e., 0.4 Myr (first column), 0.6 Myr (second column), and 0.8 Myr (third column). First row: orientation of intensity gradients in the range of  $[0, \pi)$  (i.e., red:  $\simeq \pi$ , blue:  $\simeq 0$ , and green:  $\simeq \pi/2$ ). Second row: gravitationally collapsing regions (red regions) identified from the curvature of intensity gradients. Third row: areas of the gradients' amplitude corresponding to the collapsing regions identified by intensity gradients. In the same regions, we mask the low-amplitude pixel, i.e., its corresponding amplitude is less than the global mean value.

perpendicular to the magnetic field, the velocity gradient flips its direction by 90° when self-gravity dominates over turbulence. Such changes mark the transition from a magnetic field and turbulence-dominated regime at low densities into higher-density regions that are collapsing under gravity.

Based on the change of gradients' orientations in the collapsing region, we propose two novel approaches to identify gravitational collapsing regions through velocity gradients, i.e., the double-peak algorithm (see Section 3.2) and the curvature algorithm (see Section 3.3). The double-peak algorithm quantifies the change of gradients' orientation in a histogram format. Suppose we zoom in on a subregion and draw the corresponding histogram of velocity gradients' orientation. When the subregion is diffuse, the velocity gradient will be perpendicular to the magnetic field, and the histogram will be a single Gaussian distribution. However, when the subregion contains enough collapsing materials, i.e., on the boundary of the collapsing region, some velocity gradients flip their directions by 90°, becoming parallel to the magnetic field. The histogram, therefore, appears as two Gaussian peak values at angles  $\theta$  and  $\theta + \pi/2$ , which we denote as the double-peak feature. This feature reveals the boundary of the gravitationally collapsing region without the usage of polarimetry measurements. As for the curvature algorithm, it utilizes the geometry of the velocity gradient. When the velocity gradient goes from a diffuse region to a collapsing region, i.e., on the boundary of the collapsing region, its direction is rapidly changed by 90°. This significant change induces the maximum curvature of velocity gradients, but the ambient region usually has small

curvature. The calculation of curvature, therefore, allows us to highlight the boundary of the gravitational collapsing region.

# 7.1.2. Implications for Intensity Gradients

Intensity gradients also change their direction in the presence of self-gravity (Yuen & Lazarian 2017b; Hu et al. 2019a). In particular, Hu et al. (2019a) elaborated on the difference between intensity gradients and velocity gradients in the presence of self-gravity with more numerical detail. That study clearly showed that, in self-gravitating regions, the change of intensity gradients' orientation is faster and more dramatic than that of velocity gradients. The expected reason is that the change of the density field is an accumulating process, while the velocity field is significantly changed only when the gravitational energy dominates over the kinematic energy of turbulence. Ergo, this provides a way of, first of all, locating regions dominated by self-gravity, and second, identifying the stage of gravitational collapsing.

By utilizing the properties of intensity gradients under the influence of gravity, in Section 6 we apply the tools developed in this paper, i.e., the double-peak algorithm and the curvature algorithm, to intensity gradients. We see that, in the case of gravitational collapse, intensity gradients flip their direction by 90°, and large gradients' amplitudes are induced simultaneously. It then provides a self-consistent way to identify gravitationally collapsing regions through intensity gradients. However, the change of direction was shown to happen at different stages of the collapse (Lazarian & Yuen 2018). By

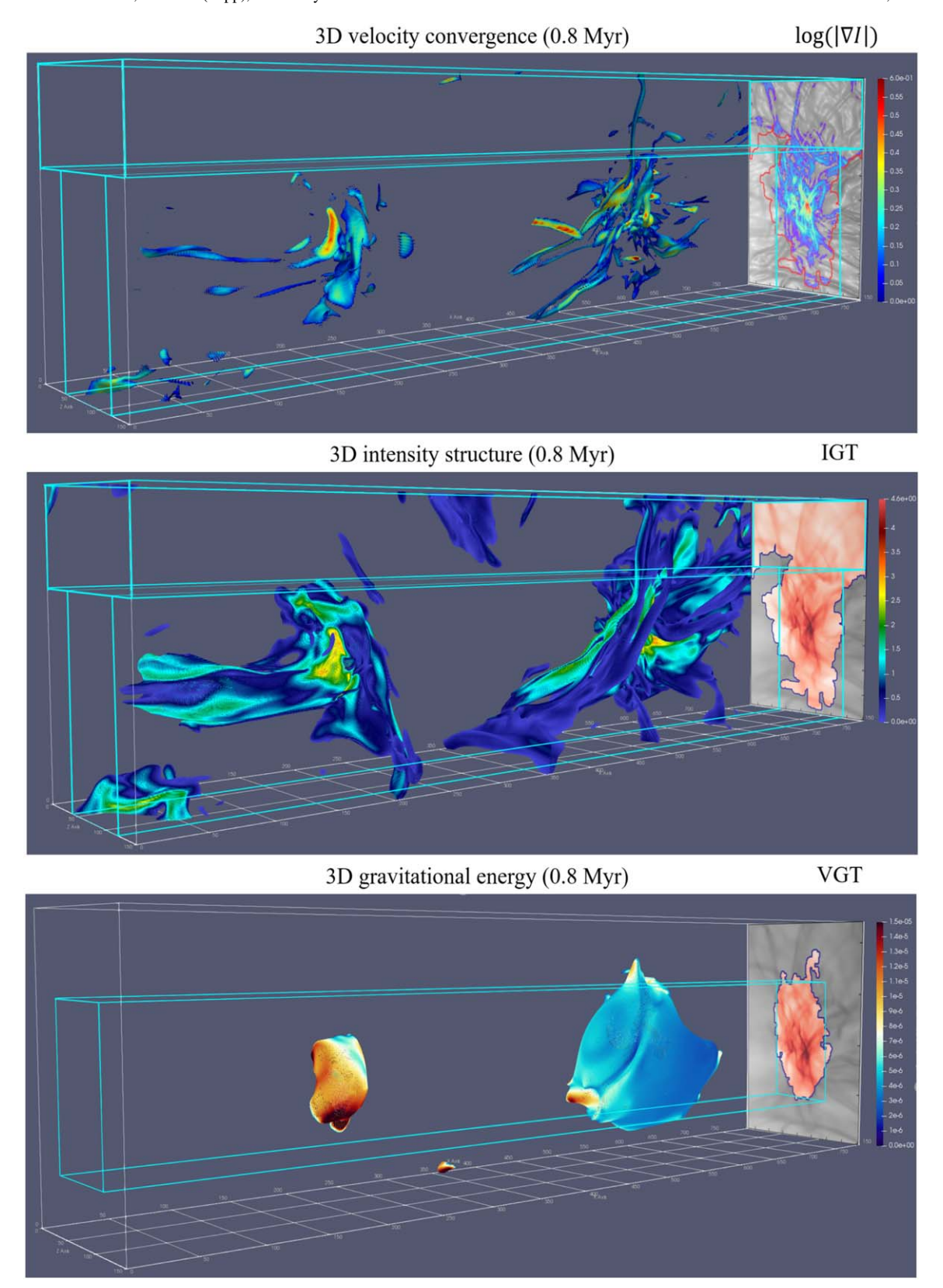


Figure 21. Top: visualization of 3D velocity convergence using simulation A1 at  $t_r \simeq 0.8$  Myr. Positive convergence outlines the convergent inflow. Inner blue box approximately outlines the boundary of the 3D collapsing region identified from IGT. Projected 2D plot on the right side shows the corresponding intensity gradients amplitude log ( $|\nabla I|$ ). We mask the low-amplitude pixel, i.e., its corresponding amplitude is less than the global mean value. Middle: visualization of 3D intensity structures. Inner blue box approximately outlines the boundary of the 3D collapsing region identified from IGT (red region in the 2D projection). We highlight high-intensity structures, i.e., their corresponding intensity is five times larger than the global mean value. Bottom: visualization of 3D gravitational energy. Inner blue box approximately outlines the boundary of the 3D collapsing region identified from VGT (red region in the 2D projection). We keep only the pixels with high gravitational energy, i.e., those with corresponding gravitational energy five times larger than the global mean value.

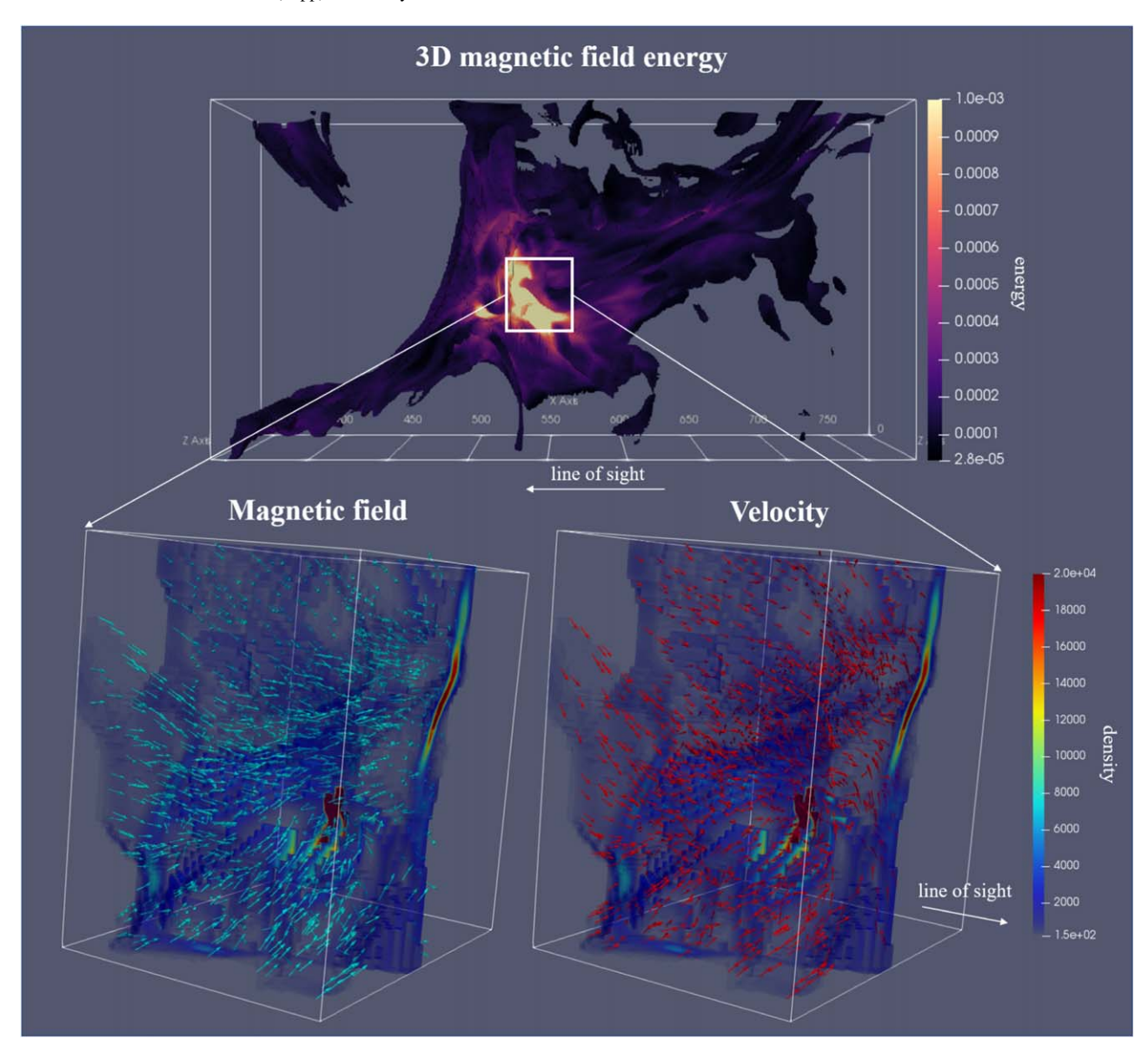


Figure 22. Top: visualization of 3D magnetic field energy using simulation A1 at  $t_r \simeq 0.8$  Myr. We highlight high-intensity structures, i.e., their corresponding intensity is five times larger than the global mean value. Bottom: visualization of magnetic field's orientation (left, blue vectors) and velocity's direction (right, red vectors). Note that this subregion exhibits high magnetic field energy and the velocity indicates the direction of convergent flow. Units of energy and volume density are  $M_{\odot}$  pc<sup>2</sup> Myr<sup>-2</sup> and  $M_{\odot}$  pc<sup>-3</sup>, respectively.

comparing the velocity and intensity gradients, one could distinguish the stage of the gravitational collapse.

# 7.2. Comparison with Other Techniques

In recent decades, several techniques have been proposed to probe magnetic field morphology based on the anisotropic properties of turbulence (see Section 2). The Correlation Function Anisotropy (CFA) technique employs the correlation function to predict the magnetic field (Esquivel & Lazarian 2005; Burkhart et al. 2014). At the same time, the CFA advantageously gives analytical predictions of different anisotropies associated with slow, fast, and Alfvén modes (Kandel et al. 2016, 2017a, 2017b). However, the CFA requires a larger statistical area for averaging than does the VGT, and thus the CFA can only estimate a coarse structure of the magnetic field (Yuen et al. 2018).

Clark et al. (2014) proposed the rolling Hough Transform (RHT) to study the magnetic field in the diffuse interstellar region probed by neutral hydrogen 21 cm emission. However, the RHT requires linear structures elongating along the magnetic field in the ISM (Clark et al. 2014). As for molecular clouds, there exist structures perpendicular to the magnetic field (Planck Collaboration et al. 2016; Soler 2019). Since RHT does not distinguish the perpendicular structures and the parallel structures with respect to the magnetic field, it is therefore incapable of revealing the magnetic field direction in the molecular cloud (Malinen et al. 2016). Compared with RHT, VGT is parameter-free (since the block size is self-consistently found) while RHT requires three parameters as inputs: a smoothing kernel diameter (DK), window diameter (DW), and intensity threshold (Clark et al. 2014). Although CFA and RHT can be complementary to the study of magnetic fields in some phases of interstellar media, neither of them can be used to identify the gravitational collapse—but VGT can.

	$\nabla v_l$ versus $B$	$\nabla \rho_l$ versus $B$	$ \nabla v_l $	$ \nabla \rho_l $
Shock	Т		Low	Low
Collapse		II	High	High

**Note.** The second and third columns show the relative orientation between gradients and the magnetic field *B*. The fourth and fifth columns indicate the gradients' amplitude.

The N-PDFs of column density is an alternative approach to study the gravitational collapse (Vazquez-Semadeni et al. 1995; Robertson & Kravtsov 2008; Ballesteros-Paredes et al. 2011; Price et al. 2011; Collins et al. 2012; Burkhart 2018). The N-PDFs, however, are strongly limited by radiation transfer effects (Hu et al. 2020a), the effects of line-of-sight contamination on the column density structure (Schneider et al. 2015a, 2015b; Law et al. 2019), and stellar feedback via ionization (Tremblin et al. 2014).

In addition to velocity gradients, intensity gradients are also widely used in the study of molecular clouds. The HRO developed in Soler et al. (2013) employs the intensity gradient to characterize the relative orientation of column density structures and magnetic fields. The HRO relies on comparison of polarimetry measurement and does not distinguish between self-gravitating regions and shocks. Also, Koch et al. (2012) uses the intensity gradient of polarized dust emission to estimate the magnetic field strength in the molecular cloud. Their technique is different: it relies on polarimetry measurement and does not take sub-block averaging, which is used in our IGT (Hu et al. 2019a).

#### 7.3. Shock Identification

The change of the direction of intensity gradients can happen in the presence of shocks (Yuen & Lazarian 2017b; Hu et al. 2019a), i.e., intensity gradients flip their direction by 90° in front of shocks, but this is not the case for velocity gradients. For instance, in Section 6, we show that the area in which intensity gradients flip their direction is significantly larger than the one seen in velocity gradients' orientation (see Figures 15 and 20). In Figure 21, we confirm that the change that happened in diffuse regions is caused by shocks. At the same, the self-gravity will induce a larger amplitude of intensity gradients than shocks. We can then separate shocks and gravitational collapse through comparison with either the intensity gradients' amplitude or velocity gradients' orientation (see Section 6). We summarize the difference between shocks and gravitational collapse in terms of the gradients in Table 2.

# 7.4. Combining Different Approaches to Trace Magnetic Fields in Star-forming Regions

Many polarimetry surveys showing the projected magnetic field morphology of molecular clouds, including the Planck survey of diffuse dust polarized emission (Planck Collaboration et al. 2018), have provided us with a comprehensive picture of magnetic field morphology across the full sky. The problem that grain alignment efficiency drops near the gravitational object center raises some concerns regarding the accuracy of such surveys (Andersson et al. 2015). It is well-known that, in

high-density regions, grain alignment frequently fails if the radiation field is not strong enough, while in the vicinity of radiation sources, the alignment can occur with respect to radiation rather than the ambient magnetic field (Lazarian & Hoang 2007; Hoang et al. 2018). Inside Giant Molecular Clouds (GMCs), this is most likely to occur in the region under severe gravitational collapse. The gravitational collapse prevents observers from studying the contribution of the magnetic field to the star formation process.

The VGT has been developed as a vast ecosystem that can not only can trace magnetic field tracing method in both the diffuse atomic gas region and dense molecular region (Hsieh et al. 2019; Hu et al. 2019b, 2019c, 2020b), it can also measure the magnetization (Lazarian & Yuen 2018; Yuen & Lazarian 2020), study the turbulent properties of the ISM, i.e., measure  $M_S$  (Yuen et al. 2018), distinguish shocks (Hu et al. 2019a), and probe the magnetic field in galaxy clusters (Y. Hu et al. 2020, in preparation). The magnetization is correlated with the dispersion of the velocity gradient's orientation. When the media is highly magnetized, the compressed gas exhibits small dispersion, while the dispersion becomes incremental for a weakly magnetized environment. The magnetization, therefore, can be computed through the power-law correlation between  $M_A$  and the dispersion given in Lazarian et al. (2018). A similar argument has also been extended to the intensity gradient by Hu et al. (2019a). In addition to the dispersion, the geometry of the velocity gradient is still sensitive to the magnetic field strength. A strong magnetic field bends the stream path formed by the velocity gradient showing small curvatures. A corresponding study, measuring  $M_A$  from the curvature, has been conducted by Yuen & Lazarian (2020). The velocity gradient also contains fruitful information about the turbulence. Supersonic turbulence induces the compressible motion of the fluid, which accordingly shows a large amplitude of the gradients, including both velocity and intensity gradients. Yuen et al. (2018) gives the power-law relation of  $M_s$  and the dispersion of the amplitude. Also, pertinent to studying the magnetic field and turbulence, one particular property of velocity gradients is that they flip their directions by 90° in the presence of gravitational collapse. This property offers two additional benefits: identifying the collapsing regions and restoring the magnetic field morphology in a self-gravitating GMC. As shown in Figure 4, we first identify the collapsing region through the double-peak algorithm and then rerotate the velocity gradients by 90°. The rerotated velocity gradients still align with the magnetic field inferred from synthetic polarization measurement, showing AM = 0.75. The comprehensive picture of the parameter-free VGT is clear. Using the molecular line observations, VGT can probe the magnetic field morphology, magnetization, and sonic Mach number over scales ranging from tens of parsecs to ≪0.1 pc, being synergistic to dust polarimetry. Once the observation has a resolution sufficiently high to resolve the collapsing structures on a scale larger than the minimum sub-block size (empirically, the minimum size is 20 × 20 pixels), VGT reveals the selfgravitating region.

To ensure the high accuracy of VGT, several approaches have been proposed to remove the noise, e.g., the Principal Component Analysis (Hu et al. 2018), and to extract the most crucial velocity gradients components, e.g., the sub-block averaging method (Yuen & Lazarian 2017a) and moving window (Lazarian & Yuen 2018). In this work, based on our

old sub-block averaging method, we develop the adaptive subblock averaging method, which guarantees the high resolution of VGT. The uncertainty of VGT measurement can also be accurately quantified through the standard deviation of velocity gradients' orientation in each sub-block. Compared with polarimetry, VGT shows advantages in probing the local magnetic fields by getting rid of the contribution along the LOS with high resolution. Besides the study of GMC, VGT can then assist in modeling the three-dimensional Galactic magnetic fields, which is indispensable for removing the Galactic foreground and detecting primordial B-mode polarization in the CMB. Our prior works have applied VGT to the full data of the GALFA-HI survey and show good correspondence, including both magnetic field tracing and E/B modes decomposition, with those reported by Planck 353 GHz (Hu et al. 2020b).

# 7.5. Observational Application of VGT

The development of the VGT was initially motivated by studying magnetic fields in turbulent diffuse gas. In molecular clouds, it was shown that the velocity gradients change their directions with respect to the magnetic field (Yuen & Lazarian 2017b; Lazarian & Yuen 2018; Hu et al. 2019c). However, the identification of these regions with polarimetry devalued the VGT technique, which is the technique of tracing the magnetic field on its own. This paper provides a detailed study of how the VGT can be used for tracing magnetic fields in self-gravitating molecular clouds. In addition to magnetic field tracing, the VGT is shown to be able to identify the collapsing self-gravitating regions. The problem of identifying such regions is significant for the understanding of star formation.

The abundant spectroscopic data sets of different molecular tracers, for instance, the CO data obtained from JCMT (Liu et al. 2019), GAS (Kauffmann et al. 2017), COMPLETE (Ridge et al. 2006), FCRAO (Young et al. 1995), ThrUMMS (Barnes et al. 2015), CHaMP (Yonekura et al. 2005), and MALT90 (Foster et al. 2011) surveys, extends the applicability of VGT. Hu et al. (2019b) showed VGT could construct the 3D magnetic field model in molecular clouds by utilizing different emission lines of Vela C molecular cloud. For example, using <sup>12</sup>CO, <sup>13</sup>CO, and C18O data, VGT tells us about the POS component of the magnetic field over three different volume density ranges, from  $10^2$  to  $10^4$  cm<sup>-3</sup>. VGT is also applicable to higher-density tracers, such as CS, HCN, HCO+ (Hu et al. 2019b). We can, therefore, expect that VGT can reveal the volume density range in which the collapsing occurs using multiple emission lines. A similar argument also holds for intensity gradients.

# 8. Summary

The paper furthers the advancement of the VGT and extends it to regions where the effect of self-gravity is important. We attempt to solve two interrelated problems. First, we explore the ability of gradients to trace of the magnetic field in the presence of gravitational collapse. In parallel, we study how to observationally identify different stages of the gravitational collapse. In our study, we present star formation simulations for different magnetization levels of the media as well as different levels of turbulence. We observe that star formation can successfully happen in strongly magnetized media and that nonideal effects like ambipolar diffusion are not necessary for this. In our simulations, after the gravitational collapse begins,

the dispersion of intensity N-PDFs, as well as the  $M_S$ , increase with the supersonic turbulence driven by self-gravity. Our main discoveries are:

- 1. We confirm that intensity gradients and velocity gradients flip their orientation by 90° in the presence of gravitational collapse, becoming parallel to magnetic fields.
- Further developing the VGT, we introduce a new adaptive sub-block averaging method that increases the resolution of the magnetic field map we obtain with our technique. We test it using the synthetic data from MHD simulations.
- 3. We demonstrate that, without polarization measurements, VGT is capable of identifying regions of gravitational collapse through:
  - (a) The double-peak feature in the histogram of gradients' orientation, i.e., in the boundary of collapsing regions, the histogram shows two Gaussian distribution with peak values  $\theta$  and  $\theta \pm \pi/2$ .
  - (b) The curvature of velocity gradients, which reaches its maximum value in a gravitationally collapsing region because intensity gradients and velocity gradients rapidly change their direction by 90°.
  - (c) The synergetic utilization of velocity gradients' morphology and amplitude that can reveal the inflow motion in collapsing regions.
- 4. We demonstrate the VGT's ability in tracing magnetic fields in both diffuse and gravitational collapsing regions.
- 5. We demonstrate the ability of VGT to reveal the boundaries of the transitional regions and determining the density range for which the gravitational collapse takes place.
- 6. Comparing the VGT to the analysis of N-PDFs, we demonstrate that N-PDFs are sensitive to the strongly convergent flows induced by the already formed accreting cores. The density threshold given by N-PDFs does not distinguish self-gravitating gas and non-self-gravitating density enhancement, while VGT traces all gravityinduced converging flow.
- 7. We explore the synergy of the VGT and its offshoot, the IGT, to identify shocks as well as different stages of the gravitational collapse.

We acknowledge Siyao Xu and Ka Wai Ho for fruitful discussions. We thank the reviewer for numerous suggestions for improving the manuscript. A.L. acknowledges the support of the NSF through grants AST 1715754 and 1816234. K.H.Y. acknowledges the support of the NSF through grant AST 1816234. Y.H. acknowledges the support of NASA TCAN 144AAG1967. We acknowledge the allocation of computer time by NERSC TCAN 144AAG1967 and the Center for High Throughput Computing (CHTC) at the University of Wisconsin.

Software: Julia (Bezanson et al. 2012), ZEUS-MP/3D (Hayes et al. 2006), Paraview (Ahrens et al. 2015).

# Appendix The Relative Angle between Magnetic Field and Line of Sight

As above, in both the strong magnetic field and weak magnetic field environments, the convergent flow induced by the gravitational collapse follows the magnetic field direction. As a result, the convergent flow significantly modifies the

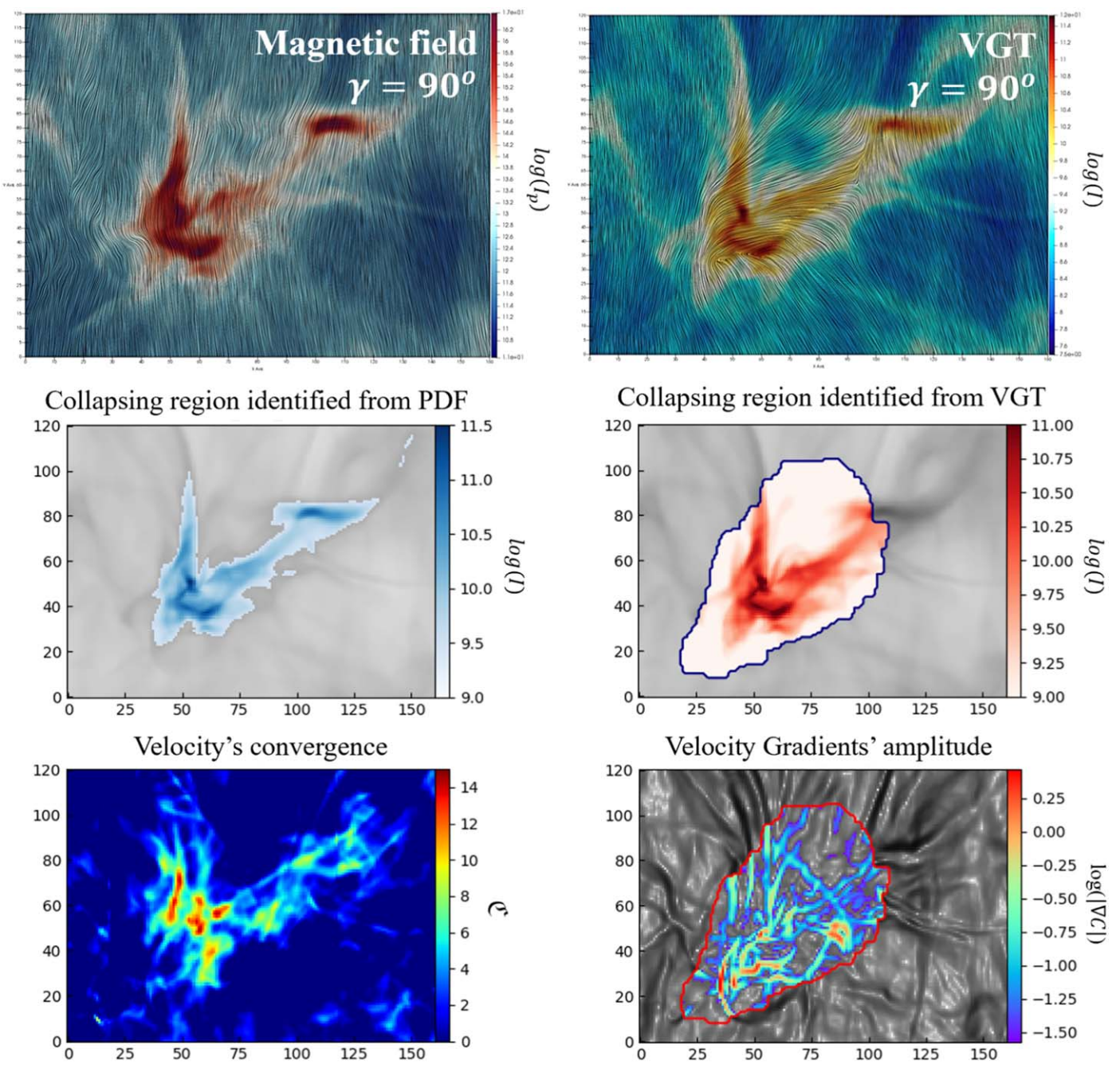


Figure A1. Example of how the VGT identifies collapsing regions from the double-peak algorithm, when the global magnetic field is perpendicular to the line of sight. We use simulation A3 with  $t_r \simeq 1.0$  Myr and length scale  $\simeq 1.96$  pc. Top right: magnetic field morphology inferred from VGT. Magnetic field is superimposed on the projected intensity map and visualized using the LIC. Here,  $\gamma$  is the relative angle between the mean magnetic field and LOS. Top left: magnetic field morphology inferred from synthetic polarization, which is superimposed on the polarized intensity map. Middle left: gravitationally collapsing regions (blue regions) identified from the N-PDFs. Middle right: collapsing regions identified by the double-peak algorithm velocity gradients with a second block size of 30. Bottom left: projected velocity convergence. Bottom right: areas (red contour) of the velocity gradient's amplitude corresponding to the collapsing regions identified by the double-peak algorithm. In the same regions, we mask the low-amplitude pixel, i.e., its corresponding amplitude is less than the global mean value.

properties of velocity gradients such that their direction becomes parallel to the magnetic field and they exhibit a larger amplitude (see Section 2).

Nevertheless, in observations, one can only ascertain the velocity component parallel to LOS. Ideally, if the flow induced by the gravitational collapse is exactly perpendicular to LOS and the flow does not allow the transfer of energy between different components, the change of velocity gradient may not be observed. However, as discussed in Section 2.4, in reality, the gravitational collapse accelerates the turbulent flow in all directions, changing

all the components of velocity. For example, in our sub-Alfvénic numerical simulation, the magnetic field is set to be perpendicular to LOS, which indicates that the convergent flow ideally should lie on the POS. However, as shown in Figure 22, near the collapse region, gravity bends the magnetic field such that all velocity components converge. The emission lines therefore always contain velocity information about the gravitational collapse. To test how the relative angle between the magnetic field and LOS affects VGT, we use a new MHD simulation A3 with  $M_s \simeq 6.47$ ,  $M_A \simeq 0.61$ ,  $\beta \simeq 0.018$ , and resolution 792<sup>3</sup>. We consider the

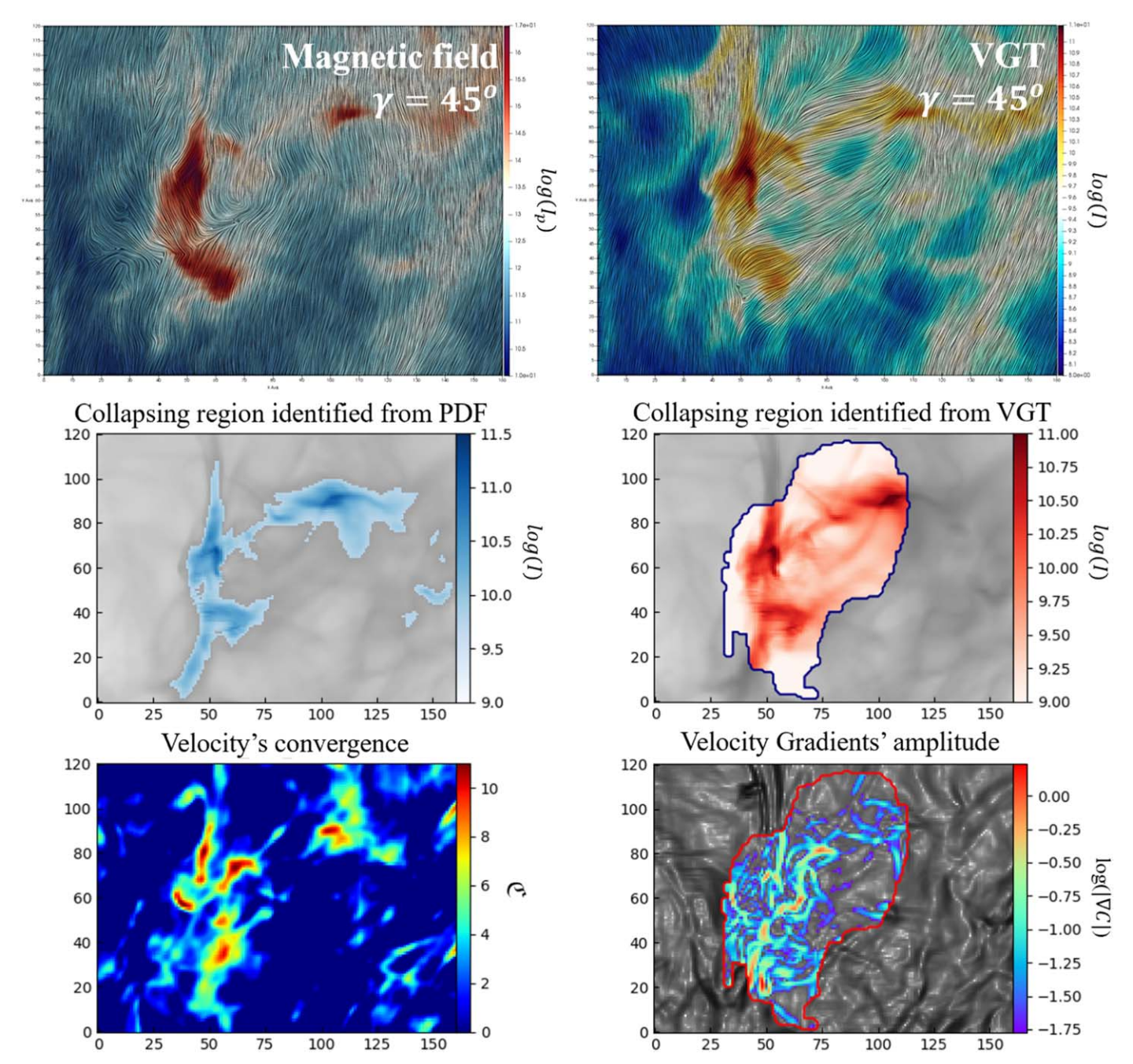


Figure A2. Example of how the VGT identifies collapsing regions from the double-peak algorithm, when the mean magnetic field is  $45^{\circ}$  inclined to the line of sight. We use simulation A3 with  $t_r \simeq 1.0$  Myr and length scale  $\simeq 1.96$  pc. Top right: magnetic field morphology inferred from VGT. Magnetic field is superimposed on the projected intensity map and visualized using the LIC. Here,  $\gamma$  is the relative angle between the mean magnetic field and the LOS. Top left: magnetic field morphology inferred from synthetic polarization, which is superimposed on the polarized intensity map. Middle left: gravitationally collapsing regions (blue regions) identified from the N-PDFs. Middle right: collapsing regions identified by the double-peak algorithm velocity gradients with a second block size of 30. Bottom left: projected velocity convergence. Bottom right: areas (red contour) of the velocity gradient's amplitude corresponding to the collapsing regions identified by the double-peak algorithm. In the same regions, we mask the low-amplitude pixel, i.e., its corresponding amplitude is less than the global mean value.

simulation at  $t_r \simeq 1.0$  Myr snapshot to have the VGT best matching the N-PDFs, as Figure 15 shows the N-PDFs are not sensitive to the initial stages of gravitation collapse. A3 is still isothermal, with temperature T = 10.0 K, sound speed  $c_s = 187$  m s<sup>-1</sup>, and cloud size L = 10 pc. The total mass  $M_{\rm tot}$  in the simulated cubes A3 is  $M_{\rm tot} \sim 8191.45$   $M_{\odot}$ , the magnetic Jean mass is  $M_{\rm JB} \sim 143.57$   $M_{\odot}$ , average magnetic field strength is  $B \sim 14.18$   $\mu$ G, mass-to-flux ratio is  $\Phi \sim 1.06$ , volume density is  $\rho \sim 141.47$  cm<sup>-3</sup>, and freefall time is  $t_{\rm ff} \sim 2.82$  Myr. As with the simulation described in Section 4, we keep driving both

turbulence and self-gravity until the simulation violates the Truelove criterion (Truelove et al. 1997). The Jeans length  $\sim\!1.77\,\mathrm{pc}$ , therefore, occupies 140 pixels. The density can be enhanced by a factor of  $\sim\!1225.0$ , i.e., we can have maximum volume density  $\rho_{\mathrm{max}}\sim173300.75\,\mathrm{cm}^{-3}$ , which informs us when to stop the simulation before having numerical artifacts due to self-gravitational collapse.

In Figure A1, we set the global magnetic field perpendicular to LOS and zoom in on subregion A3-1 from the simulation A3. This subregion contains well-defined convergent flows and

formed cores. We plot the magnetic field morphology predicted by synthetic dust polarization and VGT. We observed in the high-density regions that the rotated velocity gradients are perpendicular to the magnetic field rather than aligned with it. According to our study presented in Section 5, this is potentially a gravitational collapsing region. Through the density threshold determined from the N-PDFs, we highlight the region in which the N-PDFs is a power-law distribution, indicating this region is under gravitational collapse. We find that the collapsing region identified from N-PDFs agrees with the one showing a 90° change of velocity gradient. There is one exception: in the top right region, in which the N-PDFs indicate gravitational collapse, there is no change of velocity gradient observed. Possible explanations for this include: (i) the density threshold given by N-PDFs does not distinguish self-gravitating gas and non-self-gravitating density enhancement; (ii) the fraction of collapsing material is so small in this region that the velocity gradient does not reveal its existence (see the discussion in Section 3.2). Nevertheless, we apply the double-peak algorithm with the second block size set to 30 in order to identify the collapsing regions from the velocity gradient (see Figure A1). First, we observe that the majority of self-gravitating regions identified from the two methods, i.e., N-PDFs, and VGT, are similar and reflect the convergent flows. However, VGT shows larger identified areas than do the N-PDFs, since the double peak is required to cover both the diffuse and self-gravitating regions in order to identify the boundary. To reduce the boundary effect, we highlight the region showing a high amplitude of gradients, i.e., its corresponding amplitude is larger than the global mean value. Since the gravitational collapse also induces a high amplitude in the gradients (see Section 5), this procedure helps exclude the additional diffuse regions introduced by the double-peak algorithm.

The above result illustrates the case where the global magnetic field is perpendicular to LOS. We then rotate the MHD simulation A3 so that the magnetic field is 45° inclined to LOS. The corresponding convergent flow is changed together with the magnetic field. We repeat the calculation of VGT as above. The results are presented in Figure A2. We can see that, for the low-density regions, the magnetic field morphology inferred from VGT agrees well with the one derived from synthetic polarization measurement. For the intermediate regions, however, the velocity gradient starts appearing misaligned with the magnetic field. This misalignment comes from the spread convergent flow in the space, because the inclination angle  $\gamma = 45^{\circ}$ . Insufficient collapsing material along the LOS will also induce a change of velocity gradient, but this change does not arrive at 90°. Nevertheless, in high-density regions, the VGT measurement becomes perpendicular to the magnetic field and the magnetic field is also partially bent by the self-gravity, as we see in Figure 22. We can see that this high-density region corresponds to the collapsing region determined by N-PDFs. By repeating the double-peak and gradient amplitude algorithm, we obtain results similar to those from the N-PDFs, and we also determine the convergent flow. Thus, we conclude that the relative angle between the magnetic field and LOS does not degrade the VGT.

# **ORCID iDs**

Yue Hu https://orcid.org/0000-0002-8455-0805

#### References

```
Ahrens, J., Geveci, B., & Law, C. 2015, EnUK, 836, 717
Andersson, B.-G., Lazarian, A., & Vaillancourt, J. E. 2015, ARA&A, 53, 501
Ballesteros-Paredes, J., Klessen, R. S., mac Low, M.-M., & Vazquez-Semadeni, E.
   2007, in Protostars and Planets V, ed. B. Reipurth, D. Jewitt, & K. Keil
   (Tucson, AZ: Univ. Arizona Press), 63
Ballesteros-Paredes, J., Vázquez-Semadeni, E., Gazol, A., et al. 2011,
   MNRAS, 416, 1436
Barnes, P. J., Muller, E., Indermuehle, B., et al. 2015, ApJ, 812, 6
Beresnyak, A., & Lazarian, A. (ed.) 2019, Turbulence in Magnetohydrodynamics
   (Berlin: De Gruyter)
Bezanson, J., Karpinski, S., Shah, V. B., et al. 2012, arXiv:1209.5145
Brandenburg, A., & Lazarian, A. 2013, SSRv, 178, 163
Brunt, C. M., & Heyer, M. H. 2002a, ApJ, 566, 276
Brunt, C. M., & Heyer, M. H. 2002b, ApJ, 566, 289
Burkhart, B. 2018, ApJ, 863, 118
Burkhart, B., Falceta-Gonçalves, D., Kowal, G., & Lazarian, A. 2009, ApJ,
  693, 250
Burkhart, B., Lazarian, A., Leão, I. C., et al. 2014, ApJ, 790, 130
Caprioli, D., & Spitkovsky, A. 2014, ApJ, 783, 91
Chepurnov, A., & Lazarian, A. 2009, ApJ, 693, 1074
Chepurnov, A., Lazarian, A., Santos de Lima, R., & Appleby, S. 2020,
   arXiv:2004.03514
Cho, J., & Vishniac, E. T. 2000, ApJ, 539, 273
Clark, S. E., & Hensley, B. S. 2019, ApJ, 887, 136
Clark, S. E., Peek, J. E. G., & Miville-Deschênes, M.-A. 2019, ApJ, 874, 171
Clark, S. E., Peek, J. E. G., & Putman, M. E. 2014, ApJ, 789, 82
Clarke, S. D., Whitworth, A. P., Spowage, R. L., et al. 2018, MNRAS,
   479, 1722
Collins, D. C., Kritsuk, A. G., Padoan, P., et al. 2012, ApJ, 750, 13
Coolidge, J. L. 1952, The American Mathematical Monthly, 59, 375
Crutcher, R. M., Wandelt, B., Heiles, C., et al. 2010, ApJ, 725, 466
Dickey, J. M., McClure-Griffiths, N. M., Stanimirović, S., Gaensler, B. M., &
   Green, A. J. 2001, ApJ, 561, 264
Elmegreen, B. G., & Scalo, J. 2004, ARA&A, 42, 211
Esquivel, A., & Lazarian, A. 2005, ApJ, 631, 320
Esquivel, A., Lazarian, A., Pogosyan, D., et al. 2003, MNRAS, 342, 325
Federrath, C., & Klessen, R. S. 2012, ApJ, 761, 156
Federrath, C., & Klessen, R. S. 2013, ApJ, 763, 51
Foster, J. B., Jackson, J. M., Barnes, P. J., et al. 2011, ApJS, 197, 25
Galtier, S., Nazarenko, S. V., Newell, A. C., et al. 2000, JPlPh, 63, 447
Goldreich, P., & Sridhar, S. 1995, ApJ, 438, 763
González-Casanova, D. F., & Lazarian, A. 2017, ApJ, 835, 41
González-Casanova, D. F., & Lazarian, A. 2019, ApJ, 874, 25
Hayes, J. C., Norman, M. L., Fiedler, R. A., et al. 2006, ApJS, 165, 188
Hennebelle, P., & Chabrier, G. 2011, ApJL, 743, L29
Hoang, T., Cho, J., & Lazarian, A. 2018, ApJ, 852, 129
Hsieh, C.-H., Hu, Y., Lai, S.-P., et al. 2019, ApJ, 873, 16
Hu, Y., Ho, K. W., Yuen, K. H., et al. 2020a, ApJ, submitted (arXiv:2001.
Hu, Y., Yuen, K. H., & Lazarian, A. 2018, MNRAS, 480, 1333
Hu, Y., Yuen, K. H., & Lazarian, A. 2019a, ApJ, 886, 17
Hu, Y., Yuen, K. H., & Lazarian, A. 2020b, ApJ, 888, 96
Hu, Y., Yuen, K. H., Lazarian, A., et al. 2019b, ApJ, 884, 137
Hu, Y., Yuen, K. H., Lazarian, V., et al. 2019c, NatAs, 3, 776
Hull, C. L. H., Plambeck, R. L., Bolatto, A. D., et al. 2013, ApJ, 768, 159
Jokipii, J. R. 1966, ApJ, 146, 480
Kandel, D., Lazarian, A., & Pogosyan, D. 2016, MNRAS, 461, 1227
Kandel, D., Lazarian, A., & Pogosyan, D. 2017a, MNRAS, 464, 3617
Kandel, D., Lazarian, A., & Pogosyan, D. 2017b, MNRAS, 470, 3103
Kauffmann, J., Pillai, T., Zhang, Q., et al. 2017, A&A, 603, A89
Kennicutt, R. C., Jr. 1998a, ARA&A, 36, 189
Kennicutt, R. C., Jr. 1998b, ApJ, 498, 541
Khalil, A., Joncas, G., Nekka, F., Kestener, P., & Arneodo, A. 2006, ApJS,
   165, 512
Klessen, R. S. 2000, ApJ, 535, 869
Koch, P. M., Tang, Y.-W., & Ho, P. T. P. 2012, ApJ, 747, 79
Körtgen, B., Federrath, C., & Banerjee, R. 2019, MNRAS, 482, 5233
Kritsuk, A. G., Norman, M. L., & Wagner, R. 2011, ApJL, 727, L20
Krumholz, M. R., & McKee, C. F. 2005, ApJ, 630, 250
Larson, R. B. 1981, MNRAS, 194, 809
Law, C. Y., Li, H.-B., & Leung, P. K. 2019, MNRAS, 484, 3604
Lazarian, A. 2006, ApJL, 645, L25
Lazarian, A. 2007, JQSRT, 106, 225
Lazarian, A. 2009, SSRv, 143, 357
```

```
Lazarian, A., Eyink, G. L., Jafari, A., et al. 2020, PhPl, 27, 012305
Lazarian, A., & Hoang, T. 2007, MNRAS, 378, 910
Lazarian, A., & Pogosyan, D. 2000, ApJ, 537, 720
Lazarian, A., & Pogosyan, D. 2004, ApJ, 616, 943
Lazarian, A., Pogosyan, D., Vázquez-Semadeni, E., et al. 2001, ApJ, 555, 130
Lazarian, A., & Vishniac, E. T. 1999, ApJ, 517, 700
Lazarian, A., & Yuen, K. H. 2018, ApJ, 853, 96
Lazarian, A., Yuen, K. H., Ho, K. W., et al. 2018, ApJ, 865, 46
Li, G.-X. 2018, MNRAS, 477, 4951
Li, H.-B., & Henning, T. 2011, Natur, 479, 499
Li, P. S., McKee, C. F., & Klein, R. I. 2015, MNRAS, 452, 2500
Liu, J., Qiu, K., Berry, D., et al. 2019, ApJ, 877, 43
Lu, Z., Lazarian, A., & Pogosyan, D. 2020, MNRAS, 496, 2868
Malinen, J., Montier, L., Montillaud, J., et al. 2016, MNRAS, 460, 1934
Maron, J., & Goldreich, P. 2001, ApJ, 554, 1175
McKee, C. F., & Ostriker, E. C. 2007, ARA&A, 45, 565
Padoan, P., & Nordlund, A. 1999, ApJ, 526, 279
Padoan, P., & Nordlund, A. 2011, ApJ, 730, 40
Padoan, P., Haugbølle, T., Nordlund, Å., et al. 2017, ApJ, 840, 48
Padoan, P., Juvela, M., Kritsuk, A., & Norman, M. L. 2006, ApJL, 653, L125
Parker, E. N. 1965, ApJ, 142, 584
Parker, E. N. 1979, Cosmical Magnetic Fields: Their Origin and their Activity
   (Oxford: Clarendon), 858
Pattle, K. 2019, NatAs, 3, 692
Planck Collaboration, Ade, P. A. R., Aghanim, N., et al. 2016, A&A,
   586, A138
Planck Collaboration, Akrami, Y., Ashdown, M., et al. 2018, A&A, in press
   (arXiv:1801.04945)
Price, D. J., Federrath, C., & Brunt, C. M. 2011, ApJL, 727, L21
```

Ridge, N. A., di Francesco, J., Kirk, H., et al. 2006, AJ, 131, 2921

```
Robertson, B. E., & Kravtsov, A. V. 2008, ApJ, 680, 1083
Schneider, N., Csengeri, T., Klessen, R. S., et al. 2015a, A&A, 578, A29
Schneider, N., Ossenkopf, V., Csengeri, T., et al. 2015b, A&A, 575, A79
Shu, F., Najita, J., Ostriker, E., et al. 1994, ApJ, 429, 781
Shu, F. H. 1977, ApJ, 214, 488
Shu, F. H. (ed.) 1992, The Physics of Astrophysics. Volume II: Gas Dynamics
  (Mill Valley, CA: Univ. Science Books), 493
Slyz, A. D., Devriendt, J. E. G., Bryan, G., et al. 2005, MNRAS, 356, 737
Soler, J. D. 2019, A&A, 629, A96
Soler, J. D., Beuther, H., Rugel, M., et al. 2019, A&A, 622, A166
Soler, J. D., & Hennebelle, P. 2017, A&A, 607, A2
Soler, J. D., Hennebelle, P., Martin, P. G., et al. 2013, ApJ, 774, 128
Stanimirović, S., & Lazarian, A. 2001, ApJL, 551, L53
Traficante, A., Fuller, G. A., Duarte-Cabral, A., et al. 2020, MNRAS,
  491, 4310
Tremblin, P., Schneider, N., Minier, V., et al. 2014, A&A, 564, A106
Truelove, J. K., Klein, R. I., McKee, C. F., et al. 1997, ApJL, 489, L179
Vazquez-Semadeni, E. 1994, ApJ, 423, 681
Vazquez-Semadeni, E., Passot, T., & Pouquet, A. 1995, ApJ, 441, 702
Xu, S., Ji, S., & Lazarian, A. 2019, ApJ, 878, 157
Xu, S., & Lazarian, A. 2020, ApJ, 890, 157
Yonekura, Y., Asayama, S., Kimura, K., et al. 2005, ApJ, 634, 476
Young, J. S., Xie, S., Tacconi, L., et al. 1995, ApJS, 98, 219
Yuen, K. H., Chen, J., Hu, Y., et al. 2018, ApJ, 865, 54
Yuen, K. H., Hu, Y., Lazarian, A., et al. 2019, arXiv:1904.03173
Yuen, K. H., & Lazarian, A. 2017a, ApJL, 837, L24
Yuen, K. H., & Lazarian, A. 2017b, arXiv:1703.03026
Yuen, K. H., & Lazarian, A. 2018, ApJ, submitted (arXiv:1802.00024)
Yuen, K. H., & Lazarian, A. 2020, ApJ, submitted (arXiv:2002.01926)
Zhang, H., Chepurnov, A., Yan, H., et al. 2020, NatAs, 129, in press
```